



School of Chemistry

Metal Oxide Diamond Termination as a Route to Low Work Function Surfaces

Jane Geldard

**This thesis is submitted in partial fulfilment of the requirements for the
Honours Degree of BSc at the University of Bristol**

Supervisor: Professor Paul May
Second Assessor: Dr Neil Fox
Physical and Theoretical Group

Abstract

Diamond is well known for being a wide band gap semiconductor, but can also become an outstanding semiconducting material that can be used for a wide range of applications, such as sensors, microprocessors, and thermionic diode energy converters.

Diamond is an outstanding material due to its extreme hardness and highly modifiable surface, with different terminations leading to different electron affinities of the diamond surface. Diamond can also have dopant atoms added during growth, which can change the electrical conductivity of the sample. Together, with an appropriate surface termination, diamond can become a valuable semiconductor with a low work function. Hence, diamond could be a possible source for future low energy thermionic electron emission.

The motivation behind this project was to see if titanium oxide surface terminations could induce a low work function on diamond, and so to start the project, the previously well-documented ways of increasing diamond's electrical conductivity and reducing the work function are discussed. Various other previously researched metal oxide terminations were studied to see if there were similarities to titanium. The laboratory part of the project involved growing different doped diamond using various chemical vapour deposition diamond growth techniques and testing the quality of the films via Raman spectroscopy. The sample surfaces were then terminated appropriately and the elemental composition of the surfaces was determined by analysing the core electron emission using x-ray photoelectron spectroscopy. The work function of the surfaces was determined using ultra-violet photoelectron spectroscopy work function mapping. The hydrogen and titanium oxide surfaces were tested for thermionic electron emission to see if they could work as a prospective thermionic energy conversion source.

Acknowledgements

Firstly, I would like to thank my supervisor, Professor Paul May, without whom this project would not have been possible. I would also like to thank my second assessor, Dr Neil Fox, who has provided support and advice throughout the project.

I would like to extend my genuine gratitude to Fabian Fogarty, my PhD supervisor, for his daily support (and patience!) throughout the project.

I would also like to extend my thanks to the rest of the CVD diamond group, who made the project an altogether enjoyable experience!

Table of Contents

1. Introduction.....	5
1.1. Thermionic Emission	5
1.2. Diamond Doping	6
1.3. Surface Termination.....	8
1.3.1. Hydrogen.....	8
1.3.2. Oxygen.....	9
1.4. Metal Termination	10
1.5. Alkali Metals	10
1.5.1. Lithium	11
1.5.2. Caesium.....	13
1.5.3. Others.....	13
1.6. Magnesium	13
1.7. Transition Metals	15
1.8. Aluminium	16
1.9. Project Aims.....	17
2. Experimental	18
2.1. Hot Filament CVD.....	18
2.2. Microwave Plasma CVD	19
2.3. Raman Spectroscopy.....	20
2.4. Hydrogen Termination	21
2.5. Oxygen Termination	22
2.6. NanoESCA	22
2.6.1. Annealing:	22
2.6.2. X-ray Photoelectron Spectroscopy.....	23
2.6.3. Ultraviolet Photoelectron Spectroscopy	23
2.7. Sonication Cleaning.....	24
2.8. Scanning Electron Microscopy.....	24
2.9. Titanium Deposition	24
2.10. Thermionic Electron Emission	25
3. Results and Discussion	26
3.1. Diamond growth	26
3.1.1. Hot Filament Reactor	26
3.1.2. Microwave Plasma Reactor	27
3.1.3. Comparing Hot Filament CVD against Microwave Plasma CVD	28
3.2. Raman Spectroscopy.....	28
3.3. Hydrogen Termination	32
3.4. Scanning Electron Microscopy.....	32
3.5. Bell Jar Evaporator	35
3.6. X-ray Photoelectron Spectroscopy	36
3.7. Ultra-violet Photoelectron Spectroscopy.....	39
3.8. Thermionic Electron Emission	40
4. Conclusion	42
4.1. Future Work.....	42
References	43
Appendix.....	45

1. Introduction

1.1. Thermionic Emission

Thermionic electron emission is important in many applications, such as energy conversion devices, fluorescent lamps and mass spectrometers [1,2]. Diamond is an excellent candidate for possible future energy generation technologies, such as concentrated solar thermal power, as it has the potential to have a very low work function. This means electron emission can occur at red heat temperatures. Diamond is well known for being a wide band gap electronic semiconductor with a band gap of approximately 5.5 eV, but with suitable modifications applied during diamond growth, diamond can become a source of thermionic electron emission [3]. The different modification techniques that can be applied during the growth of diamond will be discussed later.

Figure 1A illustrates the basic concept of thermionic energy conversion (TEC) using an electron emitter and collector. Thermionic emission current is generated when an emitter source at elevated temperatures emits electrons that have enough kinetic and potential energy to overcome the work function barrier, and move across to the cooler collector. The electrons lose their kinetic energy in the form of heat and use their potential energy to do “work in an external circuit” [4]. The two electrodes are under a vacuum to maximise the number of electrons hitting the colder collector by limiting the number of collisions the electrons have whilst migrating from emitter to collector [4-6].

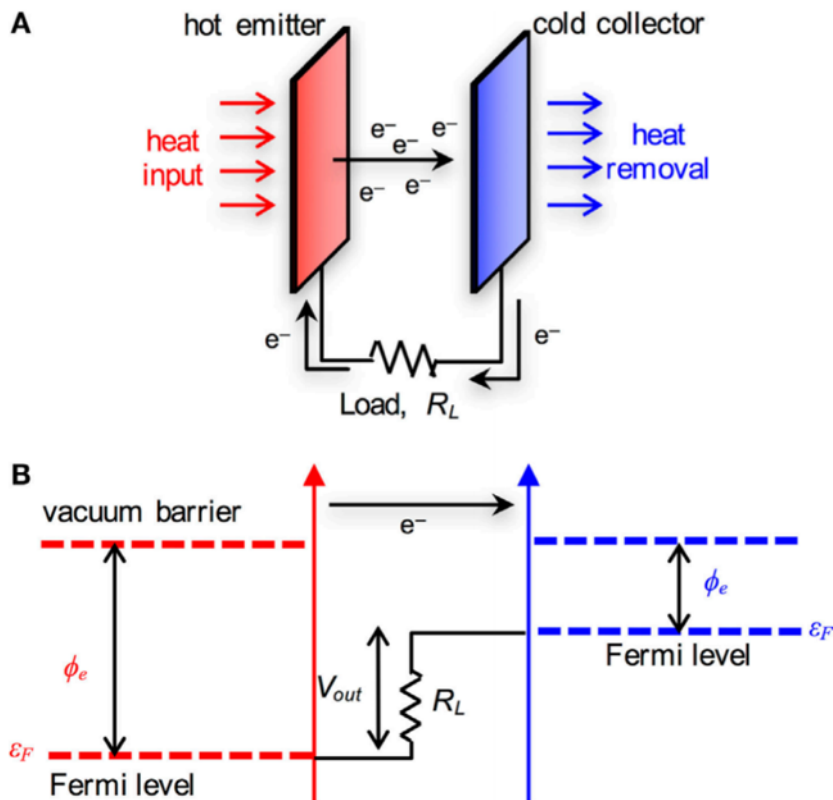


Figure 1: A) Schematic diagram of the thermionic electron emission process. B) Energy levels associated with thermionic electron emission [6].

Figure 1B shows the energy levels involved with TEC. Electrons are thermally excited from the emitter valence band to the vacuum level by overcoming the work function barrier of the emitter, ϕ_e . The work function is the energy required for an electron to be emitted from a material into the vacuum. Once emitted, the electrons then migrate across to the cold collector where the electrons have lost

thermal energy and so fall down to the collector valence band. V_{out} is the voltage output that can be determined by the difference in work functions of the two electrodes [6].

Thermionic emission depends on the heat applied to the emitter and the work function of the material. In order to make TEC as efficient as possible, a material with a low work function is required, minimising the energy input required to excite the electrons.

Diamonds can become a source for TEC by reducing the band gap between the Fermi level and the vacuum barrier. There are two widely researched methods to achieve this, adding dopant atoms which can alter the Fermi level or by changing the surface termination which can affect the electron affinity of the surface. Both methods are necessary for using diamond as a source of TEC.

1.2. Diamond Doping

Dopant atoms are purposefully added impurities used to change specific properties of the material, such as electrical and optical properties. Adding dopants can lead to new energy levels being created inside the band gap. This means that the material can become an electrical semiconductor or absorb light of visible wavelength, increasing photocatalytic activity, both giving many practical uses [7,10]. Dopants are usually added into the reaction gas mixture during the Chemical Vapour Deposition (CVD) diamond growth, allowing two different types of semiconductors to be grown; p-type and n-type. Intrinsic undoped diamond changes from having high electrical resistance to becoming electrically conducting or semiconducting upon doping. The two most common types of diamond dopants are boron doping, leading to p-type, and nitrogen doping, giving rise to n-type diamond [4,8].

Figure 2 represents a schematic diagram showing the different energy levels involved in intrinsic, p-type, and n-type diamond. As electrons become thermally excited, they vacate the valence band and start to populate the conduction band. The conduction band is where the electrons are mobile, hence becoming an electrical conductor [4,9]. The pure, intrinsic diamond is known as a wide band gap semiconductor as it has a large band gap of 5.45 eV, meaning that very few electrons are excited from the valence band maximum (VBM) to the conduction band minimum (CBM), and so does not conduct electricity [4]. In order for diamond to conduct electricity the energy gap, E_a , can be made narrower by adding dopants, so electrons can more easily access an empty band [10].

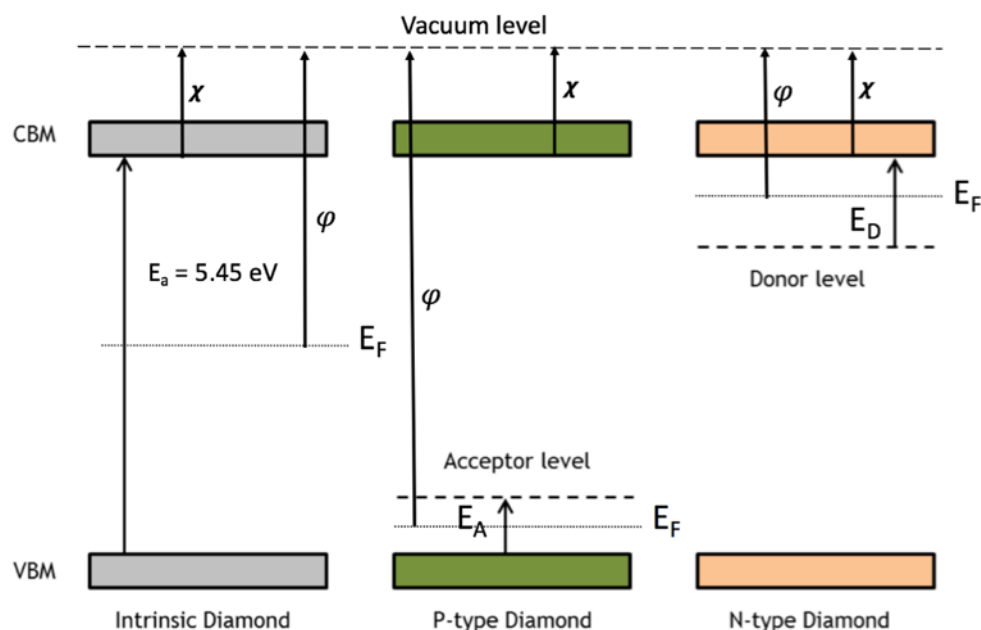


Figure 2: Schematic band diagram of intrinsic diamond, p-type diamond, and n-type diamond. VBM and CBM represent Valence Band Maximum and Conduction Band Minimum. E_F and small dashed

lines represent the Fermi level. χ and φ represent electron affinity and work function, respectively. E_a shows activation energy for an electron to move from the VBM to CBM. E_A , energy from VBM to Acceptor level and E_D , energy from Donor level to CBM. Modified from reference [4].

P-type diamond is formed by the addition of dopant atoms with fewer electrons than carbon, forming a narrow, empty acceptor energy level that lies above the VBM. This acceptor band can accept electrons from the valence band (VB), leaving positively charged ‘holes’, which allows the remaining electrons in the VB to occupy the acceptor band. P-type doped diamonds are often very electrically conducting because of the low-lying acceptor level but exhibit large work functions because of the lowered Fermi level [4,9,10].

N-type diamond is formed by the addition of dopant atoms with excess electrons, creating a narrow donor energy level below the CBM. The dopant atoms supply electrons which are free to move and are often easily excited into the conduction band (CB) because of the raised donor level, conducting electricity [4,9].

Both p-type and n-type semiconductors have reduced band gaps, meaning many more electrons can be excited from the VBM to CBM, requiring less energy to excite the electrons; hence, allowing diamond to become a useful semiconductor.

13 5 B boron 10.81	14 6 C carbon 12.01	15 7 N nitrogen 14.01	16 8 O oxygen 16.00
13 Al aluminium 26.98	14 Si silicon 28.09	15 P phosphorus 30.97	16 S sulfur 32.07

Figure 3: section of the periodic table highlighting common diamond impurities. The red highlighted boron and nitrogen are the most common p- and n-type diamond dopants, respectively. Phosphorus is also a common n-type dopant, and oxygen (along with hydrogen) are common naturally found impurities [11,12].

The most suitable dopants for diamond are similar in size to carbon as the dopants can replace the carbon in the diamond film without significantly altering the structure of the crystal. As stated earlier, the most common p-type dopant for diamond is boron, which has an acceptor level lying 0.37 eV above the VBM, meaning that boron doped diamond is able to conduct electricity at room temperature. This, however, does mean that electrons cannot be promoted into the CBM as the acceptor level contains an excess of acceptor holes [13]. Boron doping is relatively straightforward, only requiring the addition of a boron-containing gas, such as B_2H_6 , during the CVD process [14].

N-type doping with atoms larger than carbon is often more difficult due to the rigidity of the sp^3 diamond lattice [14]. Nitrogen and phosphorus are n-type dopants; nitrogen has a donor level 1.7 eV below the CB, which still requires significant energy for electron excitation into the CBM, and as a result, nitrogen doped diamond is non-conducting at room temperature. Phosphorus has a donor level at 0.5-0.6 eV below the VB, lying at a level which is high enough that electrons can be excited into the CB [4,8,13,15]. However, the radius size difference between carbon and phosphorus becomes

problematic as the substitution is not as straightforward with the larger element of phosphorus, creating non-uniform diamond films [4].

1.3. Surface Termination

The bulk of diamond contains sp^3 covalent bonds, leaving one or two ‘dangling’ bonds at the surface which need to be terminated to prevent cross-linkage, leading to graphite formation. The dangling bonds can be terminated with a range of different atoms, such as hydrogen, oxygen or metals. Surface terminations with atoms of differing electronegativities to that of carbon give rise to the surface possessing a negative or positive electron affinity.

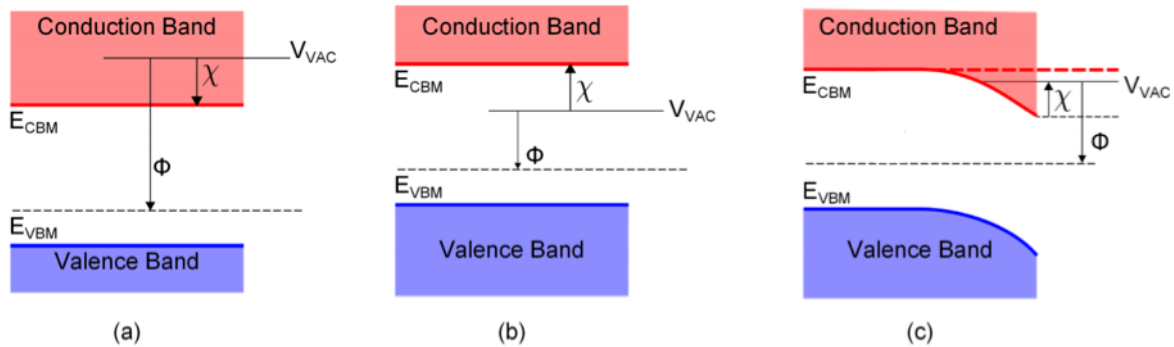


Figure 4: Schematic energy band diagram of a) a positive electron affinity, b) a ‘true’ negative electron affinity, and c) an effective negative electron affinity, where the dashed lines represent the Fermi level. V_{VAC} , E_{VBM} , and E_{CBM} represent the vacuum level, valence band maximum, and conduction band minimum, respectively. χ and Φ represent the electron affinity and work function. Modified from source [25].

Figure 4 illustrates the schematic band diagram of a semiconductor with a positive electron affinity (PEA), a true negative electron affinity (NEA), and an effective negative electron affinity (eNEA). A NEA occurs when the CBM level is higher in energy than the surrounding vacuum level, so any electrons that are excited into the CB undergo effectively barrier-less emission into the vacuum, becoming ejected from the surface. NEA occurs when the surface has a positive surface dipole with respect to the bulk, and so the bulk electron has a net attraction to the surface, reducing the amount of energy needed to escape into the vacuum. An eNEA happens when strong downwards band bending occurs at the surface of the semiconductor, allowing a PEA to act as an effective NEA. It is possible to induce an eNEA on many semiconductor surfaces, such as GaAs or doped diamond, by heavily p-doping the semiconductor, followed by covering the surface in a monolayer of a metal oxide, such as caesium oxide. The use of Cs-O and other metal oxides will be discussed in more detail later. A PEA occurs when the CBM lies below the vacuum level, meaning the electrons require additional energy to be excited into the vacuum level. PEA occurs when the negative partially charged atom lies at the outermost layer of the surface [4,21,24, 26,27].

Determination of the electron affinity of a surface is straightforward to do by exciting the VB electrons to the CBM and recording the electron emission that takes place. If an NEA is present, then there will be immediate emission and no extra energy will be required. If the surface has a PEA, extra energy will be required to emit the electrons from the CBM into the vacuum [26].

1.3.1. Hydrogen

Atomic hydrogen is extremely abundant and highly reactive during the CVD process, meaning it can quickly bond to the diamond surface, forming sp^3 hybridised bonds, keeping the structure of diamond [14,18].

Due to the difference in electronegativities of C and H, the partial charge difference builds up across the surface between the hydrogen atoms and the surface carbon atoms. This forms a dipole layer across the surface, generating a p-type semiconductor, driving the electrons from the carbon valence band to the hydrogen acceptor level [17-19,22]. As the dipole layer is formed with the outermost atom being the positive partially charged hydrogen, it has the effect of decreasing the energy of the vacuum level so that the CBM lies above the vacuum level, inducing a true NEA. Any electrons that are excited into the CB are now readily ejected into the vacuum [4]. The experimentally calculated electron affinity for a hydrogen-terminated surface is -1.3 eV which still requires significant energy input in order for the material to be used for TEC sources [25].

The major drawback to using hydrogen as a surface terminator is that it easily desorbs from the diamond surface at temperatures above 750 °C. This was demonstrated by an exponential increase in thermionic emission current until 750 °C, where the current then began to decrease. At 750 °C, hydrogen is beginning to desorb from the surface and the diamond is returning to having a wide energy gap due to the reversal of the surface dipole. At approximately 900 °C, thermionic emission current decreases to a level so low that it is no longer measurable, showing that a vast majority of the hydrogen has desorbed from the diamond surface. The sample was then cooled and re-tested for electron emission but no current was detected, showing that the majority, if not all, of the hydrogen had desorbed from the surface by 900 °C. Once the sample surface was re-covered in hydrogen by exposing the sample to a hydrogen plasma, it was re-tested for thermionic emission current. A current was observed, proving that hydrogen terminated diamond has an NEA but starts to desorb at approximately 750 °C [20,23].

Hydrogen terminated surfaces are readily oxidised when exposed to air or water, leading to a PEA. The presence of water slowly replaces hydrogen with hydroxyl groups, which changes diamond from having an NEA to a PEA, again, due to the reversal of the dipole. The same is evident with oxygen in air [21].

Doped hydrogen terminated diamond can lead to work functions between 2.85 – 3.9 eV which is still too large for thermionic emission as the hydrogen would have desorbed before appropriate temperatures were reached; hence, efficiency in TECs would be extremely poor at high temperatures [23].

1.3.2. Oxygen

Diamond is naturally oxygen terminated, or oxygen termination is easy to achieve in the laboratory using techniques such as oxygen-plasma treatment, ozonolysis or acid washing [4,22]. When the diamond surface is oxygen terminated, a PEA is induced. With an oxygen terminated diamond surface, the negative partial charge lies at the outermost of the surface due to oxygen being more electronegative than carbon. The oxygen lone pair also enhances the PEA as any electrons being emitted into the vacuum must have enough energy to overcome the electron-electron repulsion from the oxygen lone pair. This creates a build-up of charge at the surface as there is an excess of electrons lying close to the surface [4,25].

There are variations in the way oxygen can bind to the carbon surface; the two most stable binding structures are ether bridging and carbonyl, both illustrated in Figure 5. The ketone carbonyl oxygen forms a double bond to each surface carbon, as seen in Figure 5a) and the ether bridge oxygen is bound to two surface carbon atoms, as seen in Figure 5b) [25]. The ether bridging structure is slightly more stable, being 0.32 eV lower in energy than the carbonyl structure, but both configurations give a highly positive electron affinity, with experimental results of the PEA ranging from 2.63 eV to 3.75 eV, differing due to the amount of surface coverage [23].

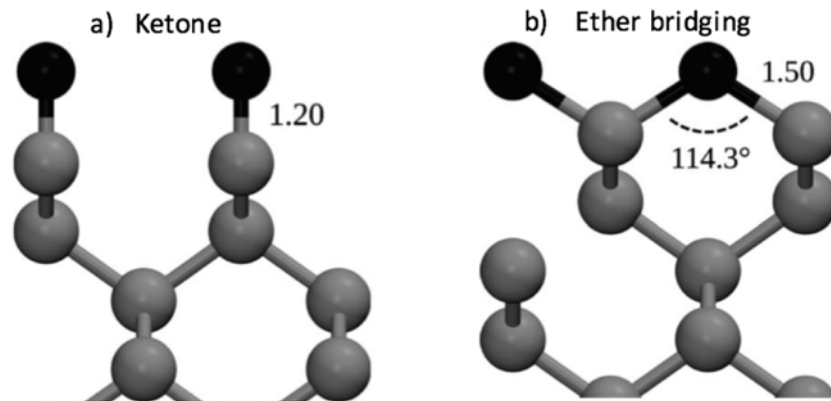


Figure 5: Optimised structures for oxygen terminated diamond – a) C(100)-(1×1):O ketone carbonyl and b) C(100)-(1×1):O ether-bridge. Lengths are shown in angstroms [23].

Oxygen stays adsorbed onto the surface at a temperature far higher than hydrogen, only beginning to desorb at approximately 1100 °C. This makes oxygen a good choice of surface termination as a metal layer can later be deposited onto the oxygen terminated diamond, inducing an NEA [23].

1.4. Metal Termination

In order to reduce the work function of doped diamond further, it is possible to induce a larger NEA by adding an electropositive metal surface layer, creating a large dipole between the metal and the oxygen or carbon atom. When considering metal or metal-oxide surface terminations there are many credible choices. The metal can be directly deposited onto the clean diamond surface or the pre-oxygen terminated diamond surface. The surface coverage from the metal can also be varied, like those seen in oxidised diamond films with the choice of carbonyl or ether bridging. Many different research groups have reported on a wide range of choice of metal to deposit, a few of which will be discussed below. Metal oxide terminations, in general, give higher binding energies and larger NEAs than metal terminations onto clean diamond, and so they will be discussed below. Described throughout this section are the possible positions where the metal can bind, which are demonstrated in Figure 6.

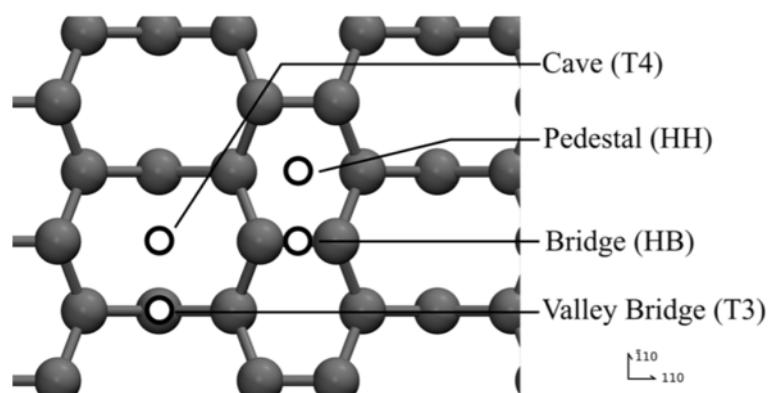


Figure 6: Plan view of the high symmetry sites suggested for possible surface adsorption onto clean diamond surface, as seen on Si(100) [23,25].

1.5. Alkali Metals

The first metal group to look at is the alkali metals, lithium through to caesium. Alkali metals are already known for reducing the work function of other semiconductors, such as GaAs and Si, and now some can be used to reduce the work function of diamond surfaces. The smaller the alkali metal, the higher the binding energy per adsorbate atom, but also a reduced electronegativity difference

between the carbon and the alkali metal. Hence, the smaller the alkali metal, the smaller the effect in decreasing the size of the effective NEA, which leads to less of an effect on reducing the work function [18]. Therefore, lithium, being the smallest alkali metal, has the least effect on reducing the work function of the X-O terminated diamond surface but the highest adsorption energy per adsorbate atom [18,23].

1.5.1. Lithium

Table 1 summarises the Density Functional Theory (DFT) calculated adsorption energies of Li deposited on clean and ether bridged oxygen terminated diamond surface. The ether bridged oxygen surface is slightly lower in energy than the ketone and so the Li-O terminated surface lowest in energy is when Li binds to the ether-bridged oxygen terminated diamond surface. There is a slight variation in the reconstruction of the diamond surface depending on which reconstruction corresponds to the lowest energy for each given surface terminators [19].

Surface	Adsorption Energy per atom (eV)	Electron Affinity (eV)
C(100)-(2×1)	-	+0.62
C(100)-(1×1):O	8.20	+2.63
C(100)-(2×1):Li	3.26	-2.70
C(100)-(2×1):LiO	4.38	-3.90

Table 1: DFT calculations for the adsorption of Li onto clean and oxygenated diamond surface. For C(100)-(2×1):LiO the adsorption energy is relative to the ether bridge O diamond surface. Showing that electron affinity ranges from +0.62 eV for the clean surface to -3.90 eV for Li on oxygenated diamond surface, showing that different surfaces can give rise to a PEA or NEA [21,23].

The carbonyl and ether-bridging structures of diamond are similar in energy, so when lithium binds to the oxygenated diamond both structures need to be considered. Due to added symmetry for the oxygenated diamond surface, there are now only two binding sites for 0.5 ML coverage, OB and OP. OB is the 2-coordinate oxygen-bridge site, made from combining the T4 cave site and HB bridge site. OP is the 4-coordinate oxygen-pedestal site, made from combining the T3 valley-bridge site and the HH pedestal site [24,25].

The Li-O bonds in both the 0.5 ML and 1.0 ML coverage do not sit normal to the surface and so a surface-centered dipole is induced, rather than an atom-centered dipole as seen with hydrogen terminated diamond. The outermost part of the surface dipole is the Li-O layer and has a positive charge, therefore an NEA is still produced [22].

Coverage (ML)	Site	Binding Energy per adsorbate (eV)		Change in Work Function (eV)	Electron Affinity (eV)
		Ketone	Ether		
0.5	OP	4.71	4.07	-2.70	-2.08
	OB	3.54		-1.87	-1.25
1.0	HH + T3	4.70	4.38	-4.52	-3.89
	HB + T3	3.90	3.76	-3.00	-2.38
	HB + T4	3.36		-2.30	-1.67

Table 2: Summary of different coverages of Li on C(100)-(1×1) surface. The lowest energy structures are recorded with the different possible oxygen binding configurations, with the work functions and electron affinities noted only for the lowest energy structure [23].

The lowest energy structure occurs when the Li atoms bind in the OP ketone position, as seen in Table 2. For 0.5 ML coverage, this results in an adsorption energy of -4.71 eV per Li atom, and an NEA of -2.08 eV, which is significant in magnitude. For both the OB and OP structures, the lowest energies occur on the ketone-bonded surface. Binding in the OB structure requires an ether-bridging bond to

break so that each C has a single O situated above, resulting in the same structure as the ketone-bonded surface. This is why for OB Li adsorption, it will most probably result in the ketone-bonded surface [25]. Figure 7 illustrates the lowest energy structures of both the 0.5 ML and 1 ML coverage on C(100)-(1×1):O.

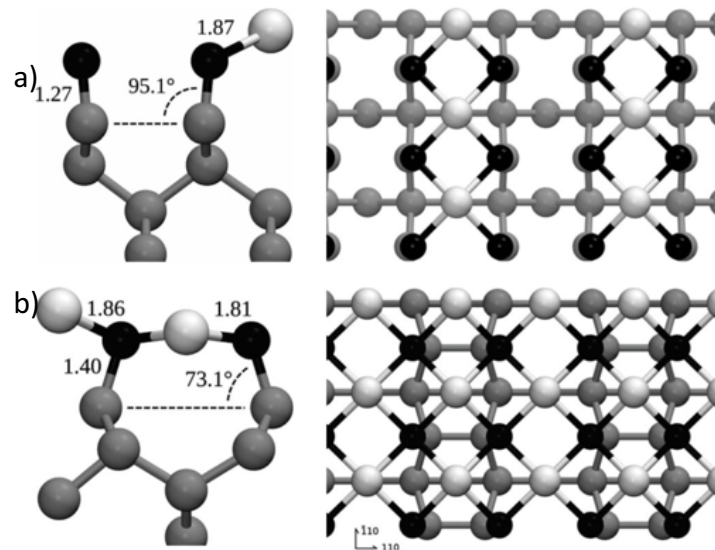


Figure 7: Lowest energy structures for a) 0.5 ML Li coverage and b) 1 ML Li coverage on C(100)-(1×1):O, with the white, black, and dark grey spheres representing lithium, oxygen, and carbon, respectively [21, 23, 25].

For 1 ML coverage, there are three unique site pairs that arise, as listed in Table 2 [23]. HH + T3 combination from ketone-bonded oxygen results in the lowest energy and so is the energetically preferred structure for 1 ML Li coverage. This leads to a work function reduction of 4.52 eV and a large binding energy of 4.70 eV per Li atom, leading to partial delocalisation of surface charges which creates a large surface dipole. This shows that 1 ML Li coverage on diamond film could be a potential device for thermionic emission sources by lowering the work function whilst still maintaining the strong binding to the surface [15,19,23,25,32].

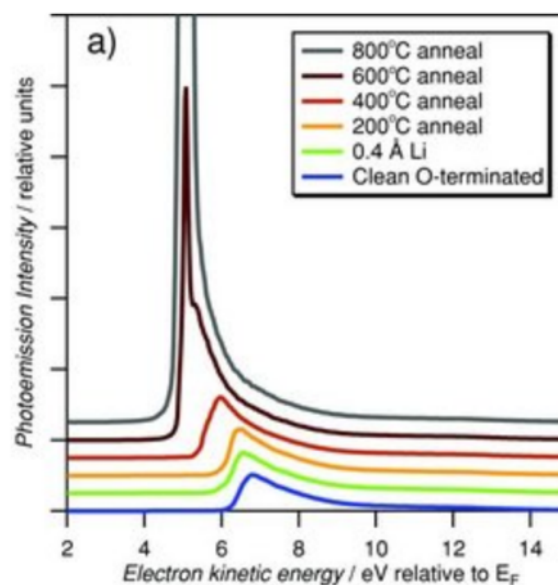


Figure 8: Graph showing how the electron kinetic energy on Li terminated diamond as the temperature of annealing increases [22].

One drawback to lithium terminated diamond is it needs to be thermally activated by annealing to give the surface an NEA. Figure 8 shows how the kinetic energy of the electron emitted changes after annealing at different temperatures. Without annealing, the Li-O termination gives rise to a slight PEA but after annealing at 600 °C for 15 minutes the sample showed an NEA. Annealing at a high temperature promotes a structural change in the way lithium is bonded to the surface. Lithium bonded to oxygen in the metastable ether-bridging site must break one of the C-O bonds in the ether-bridge to get to the more thermodynamically stable site of Li-O-C. The C-O-C bond breakage is encouraged as the annealing temperature is raised; hence, after annealing at 800 °C the sample is predominantly in the thermodynamically stable binding state, giving rise to an NEA [22,32]. The binding energies of lithium to the oxygen terminated diamond surface are large enough that Li does not desorb at temperatures up to 800 °C so Li-O terminated diamond could be a promising material for thermionic energy conversion sources.

1.5.2. Caesium

The caesium oxide surface on diamond has been extensively researched theoretically and experimentally due to its very low work function. The diamond surface, like with Li-O termination, is first oxygenated, then a layer of caesium is deposited on top. The sub-monolayer coverage of caesium on the oxygenated diamond surface creates a large conventional ionic dipole between Cs and O-C, again with the positive charge at the outermost, leading to a greatly reduced work function of 1.25 eV, which is clearly significantly lower than the 5.45 eV for intrinsic diamond [3,17,18]. Although the large size difference between Cs and O-C helps to create a larger dipole moment, it means that the binding energy per Cs atom is low, being only 1.34 eV per Cs atom. This implies the Cs-O surface is only thermally stable up to temperatures of 400°C, which is even lower than that of hydrogen terminated surfaces [18,21,23,24,29,32].

1.5.3. Others

O'Donnell *et al.* reported the adsorption of Na, K, and Rb onto the C(100)-(1x1):O diamond surface [32]. All three are large in size compared to C, therefore bind relatively weakly. The adsorption energies vary depending on surface coverage and choice of alkali metal. K and Rb, like Cs, create large classical, ionic atom-based dipoles between the positively charged metal and negatively charged oxidised diamond surface. They also exhibit a dipole between the metal site and the M-O bond. This dipole is partially cancelled out by the C-O dipole so the overall net dipole has been reduced. Na is an intermediate between the lighter and heavier alkali metals. Table 3 shows a summary of the surface coverage with the lowest adsorption energy associated with each metal. The larger the metal, the lower the coverage because of size constraints on the diamond surface [21,25,28,32]. Hence, all showing much weaker adsorption energies and less NEAs than Li-O.

Alkali metal	Coverage	Surface Unit Cell	Adsorption Energy (eV)	Electron Affinity (eV)
Na	0.50	2X2 ($\sqrt{2}\times\sqrt{2}$)	-2.41	-1.30
K	0.25	2x2	-2.44	-2.44
Cs	0.25	2x2	-2.19	-2.41

Table 3: summary of data presented by O'Donnell *et al.* displays the lowest energy coverage for a 2x2 reconstructed oxygen terminated surface [32].

1.6. Magnesium

Magnesium is similar in size to lithium and exhibits a similar electronic structure of a delocalised surface dipole, rather than an atom-centered dipole. The ether bridging bonds upon adsorption of Mg and Li are broken, creating a sizable dipole across the surface, lowering the NEA. The main difference between the two metals is that the magnesium surface does not need to be annealed at high

temperatures, unlike lithium which needs to be initially thermally activated by annealing at 600 °C, making the process for magnesium much easier [25,31].

O'Donnell *et al.* have reported that 0.50 ML coverage of Mg induces a minimum NEA of -2.00 eV, as seen in Figure 9. The NEA reduction at 0.50 ML leads to a reduced work function of 2.40 eV. As coverage increases past 0.50 ML, the electron affinity becomes less negative as there is a reduction of charge transfer and so the work function increases towards the bulk magnesium work function, approximately 3.6 eV. The initial display of an NEA with minimal Mg adsorption suggests that high temperature annealing for Mg is not required, unlike with Li [31].

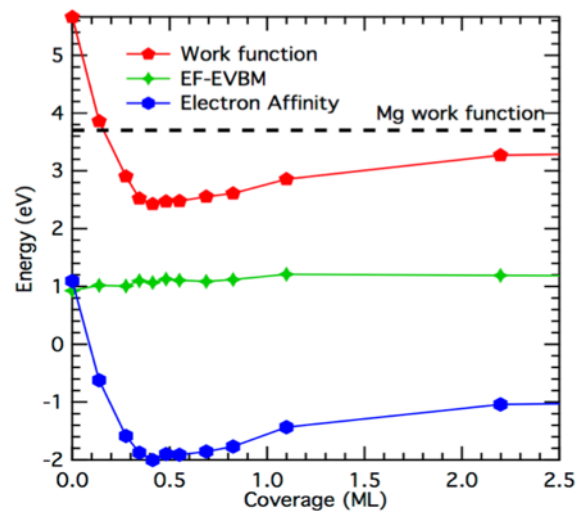


Figure 9: Change in work function, $E_F - E_{VBM}$ and electron affinity as coverage of magnesium onto oxygenated C(100) surface increases. Minimum when Mg coverage is 0.5 ML [31].

Mg and Li show similarities in bonding. The similarities come from the binding of the metal to the oxygen in which both metals lie close to the surface. This is due to the metal, oxygen, and carbon all being similar in size. Mg has a similar effect on the oxygen lone pair states as Li because the light metals lie close to the surface leading to a downshift of the VB energy as the oxygen lone pair states overlap with the VB. This leads to more covalent bonding, hence, Mg and Li have relatively strong binding energies. The heavier alkali metals do not sit as close to the surface; therefore, they have a small effect on the oxygen lone pair energy states [31,32].

Although Mg and Li show similarities in bonding and structure, the main appearance of the 0.5 ML Mg coverage surface is very different from the topography for Li coverage. The most stable structure for Mg is when the carbon surface layer reconstructs to a 2x2 surface, with one Mg atom adsorbing per unit cell [31].

With Mg, there is significant electron emission from below the conduction band minimum into the vacuum, unlike for Li adsorption. Figure 10 shows the spectrum for Mg having an E_{VAC} below the surface CBM; this is because it has a true NEA, whereas Li has an effective NEA. This means for the eNEA, significant band bending allows the bulk CBM to lie above the E_{VAC} but the surface CBM is below the E_{VAC} , hence why E_{VAC} is only shown for Mg and not Li [31,34]. Mg exhibits a large true NEA, so electrons that have been excited into the CBM can fall into unoccupied surface levels which lie in the band gap. Emission can then occur from energy levels above the vacuum energy level, and as a result, there is a spread of kinetic energies for the Mg spectrum and not Li [31].

Mg has a more gradual decline of electron emission after the CBM, whereas Li has obvious oscillations. The Mg surface does not need to be annealed to induce an NEA, which leads to slight random

variations in surface topography, hence slight variations in the magnitude of NEA. The slight variations in the NEA make the oscillations less distinct. Upon annealing, the Li-O-C surface becomes well ordered, thus, there are visible oscillations in electron emission after the CBM [31].

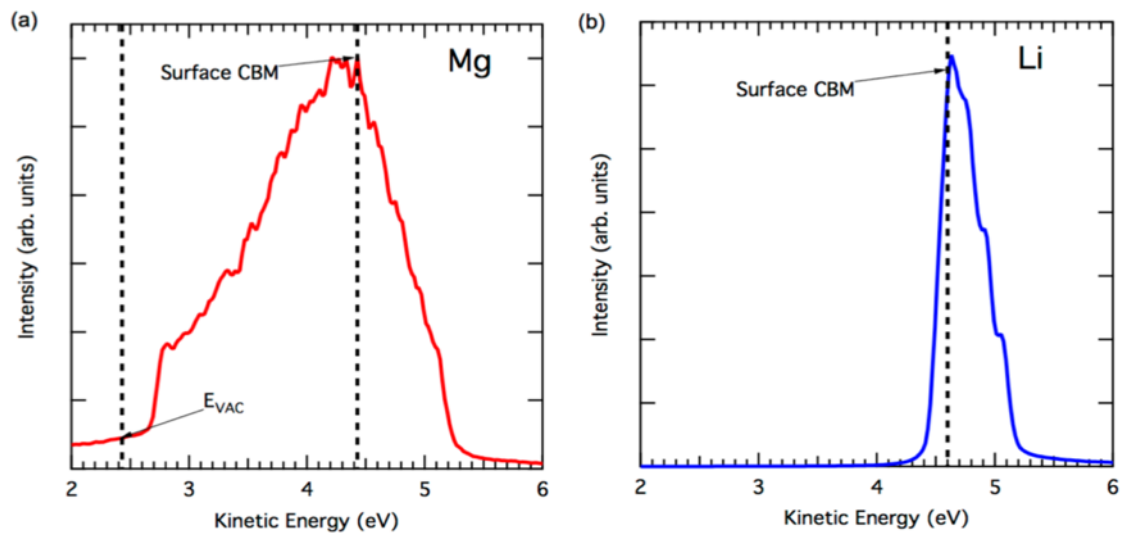


Figure 10: Kinetic emission spectrum for 0.5 ML coverage on oxygen terminated diamond for a) Mg and b) Li. The dashed lines represent the surface CBM energy levels and the vacuum energy level for Mg adsorption [31].

Mg-O terminated diamond exhibits a large NEA without needing to be annealed at high temperatures; it can withstand exposure to air or water, whilst still exhibiting an NEA. Thus, Mg-O terminated diamond looks like a promising, robust material for thermionic electron emission [31].

1.7. Transition Metals

Following on from the work of magnesium and alkali metal oxides, the adsorption of transition metals onto the oxidised diamond surface has been studied computationally to see if they induce an NEA. Many showed potential to becoming a route to low work function surfaces. In particular, Cu, Zr, Co, and Ni showed potential of exhibiting an NEA, but it has proved difficult to understand the structural and electronic configurations due to lack of experimental data [4,21]. However, theoretically, transition metal oxide (TMO) surfaces look like a promising route to diamond being used as low-temperature TEC sources due to TMO thermal stability and induction of an NEA. Tiwari *et al.* reported that the carbide forming species, Ti and Zn, induce larger NEAs, approximately 3 eV, whereas Cu and Ni only induce a small NEA.

Table 4 displays the different binding energies and electron affinities of various TMOs and the associated stoichiometries. In order for the TM to bind to the oxygenated surface, the diamond surface must reconstruct to form a $(2 \times N)$ reconstructed surface, where oxygen is monovalent. This can then result in 0.25, 0.50 and 1.0 ML TM coverage of the diamond surface, leading to M_2O , MO and MO_2 stoichiometries [29].

The magnitude of the induced NEA depends on the thickness of the layer and on the transition metal itself [19,22]. Only Ti and Zn induce a large NEA but it is clear that the adsorption energy for Ti is over 6 eV larger than Zn, showing that Ti gives the most thermally stable TMO by a long way. For Ti, the 1:4 M:O ratio results in the most energetically favourable arrangement, giving the strongest binding energy and largest NEA, -7.60 eV and -3.10 eV, respectively [22]. The Pauling electronegativities listed in Table 4 show that the two TMs with the lowest electronegativities lead to the largest NEAs, corresponding to Ti and Zn. This is due to the electropositive metals forming a larger surface dipole with O-C, attracting electrons out of the diamond bulk towards the surface [29].

Transition Metal	M:O	Surface Reconstruction $2 \times N$	Adsorption Energy (eV)	Electron Affinity (eV)	Pauling Electronegativity
Ti	1:1	1	-5.35	1.74	1.54
	1:2	1	-6.15	1.57	
	1:4	2	-7.60	-3.10	
Ni	1:1	2	-2.67	1.41	1.91
	1:2	1	-3.80	-0.16	
	1:4	2	-2.69	1.67	
Cu	1:1	1	-2.05	0.05	1.90
	1:2	1	-2.35	-1.28	
	1:4	2	0.03	1.13	
Zn	1:1	1	-1.00	0.30	1.65
	1:2	1	-1.13	-3.05	
	1:4	1	0.97	-0.40	

Table 4: Tiwari *et al.* group's calculated adsorption energies and electron affinities for different stoichiometries adsorbed onto the oxygenated C(100) surface. Bold lines represent the stoichiometry for each TM with the lowest adsorption energy [29,33].

The thickness of the layer affects the electron affinities so much that it can change the electron affinity from an NEA to a PEA. In general, thick metal coverage reduces the magnitude of the NEA. In all cases of the above metals, 1:1 M:O ratio results in a PEA because of the largely reduced charge transfer [29].

Ti-O displayed an NEA larger than hydrogen and smaller than Li-O and Mg-O, but Ti-O is much more energetically favourable, with an E_{ads} of -7.60 eV compared to Li-O, with an E_{ads} of -4.7 eV [22]. Tiwari *et al.* have reported that Ti is compatible with Schottky and Ohmic semiconductor device growth and fabrication processes, unlike Li which is not robust enough, stopping Li from being used [29].

1.8. Aluminium

James *et al.* carried out DFT calculations on aluminium deposition oxygenated C(100) diamond surface. Table 5 summarises data for variations in coverage of Al, displaying the only the structure giving the largest binding energies available, along with the associated NEA for that structure [24].

Coverage (ML)	Structure	Electron Affinity (eV)	Binding Energy per Adsorbed Al Atom (eV)
0.25	T3*OP (Ketone)	-0.37	-6.36
0.50	T3*OB (Ketone)	+1.06	-5.99
1.0	HB + T3	+0.54	-4.58

Table 5: coverage corresponding to the largest induced NEA associated with binding to oxygenated C(100) surfaces. * indicates the (1x1) reconstructed surface required to form this structure [24].

Figure 11 shows the lowest energy structures for the different coverages of Al. In this study, the ether and ketone arrangements are similar in energy. For both configurations, there are two high-symmetry positions that Al can bind; OP and OB. OP is the 4-coordinate oxygen-pedestal and OB is the 2-coordinate oxygen-bridge site. Similar to Ti, the largest binding energy is at 0.25 ML coverage, as highlighted in Table 5. This is due to size constraints of the metal lowering the binding energy of each adsorbate after 0.25 ML coverage. Al, like Ti preferentially binds in the 4-coordinate position. Al does not look as promising as Ti when looking at the DFT calculations as the only lowest energy structure for each coverage inducing an NEA is 0.25 ML, and even then, it is only a weak NEA of -0.37 eV. For

0.50 ML coverage, the minimum energy position is T3*OB (Ketone) but this leads to a PEA, rather than NEA, likewise with the 1 ML coverage. The hexagonal relaxation, as seen in Figure 11c), shows some Al atoms having to lie further from the surface, and as a consequence, have lower binding energies [24].

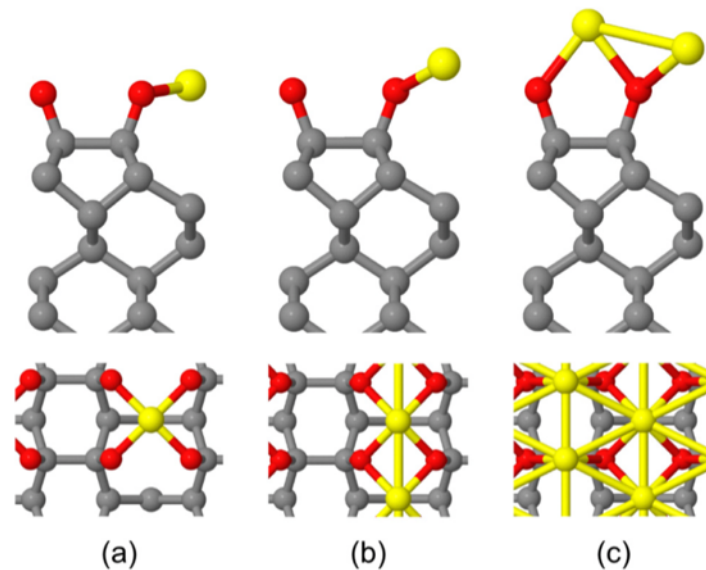


Figure 11: Lowest energy structures for a) 0.25 ML Al coverage, b) 0.5 ML Al coverage and c) 1.0 ML Al coverage on C(100):O, with added views along $\langle 100 \rangle$. Grey, red and yellow spheres represent carbon, oxygen and aluminium atoms, respectively [24].

Aluminium has similar binding energies to titanium, as both metals are of similar electronegativities and can form carbides. However, Al-O induces a much smaller NEA than Ti-O, hence, Ti-O will be researched experimentally during the laboratory project.

1.9. Project Aims

Over recent years there has been an increase of interest in finding alternatives to hydrogen termination on diamond surfaces to yield diamond with an NEA. For thermionic electron emission applications at low temperatures, work functions near to 1 eV are preferable. Hence, the solution is to find a balance between the thermal stability of the bond strength and the structure having a large dipole moment leading to a highly polar surface [17,18]. Out of all metals discussed, titanium shows to be the most promising, hence, the laboratory project is based around depositing titanium oxide onto diamond. Titanium oxide has shown to be a robust termination choice for diamond, withstanding high temperatures due to the thermal stability, but also not being readily oxidised when exposed to air or water. The possibility of having an NEA of -3.10 eV has a massive effect on reducing the work function of nitrogen doped diamond to just a few eV, showing that Ti-O terminated nitrogen doped diamond could be a serious potential contender for low temperature TEC sources in the near future. Tiwari *et al.* have predicted that Sc, Zr, and V could potentially be TMOs of interest due to the difference in electronegativities between the TM and carbon. There are also similarities to Ti in the size of TM, electronics and the thermal stability of the oxides, implying they could be similar to Ti-O terminated diamonds [29,30].

The main aims of the laboratory project are to grow nitrogen and boron doped diamonds using the required CVD techniques, terminate the surfaces appropriately, and analyse the surfaces using a variety of techniques. The second part will involve the deposition of titanium and determine the work function for different coverage amounts and see if any could be a potential for thermionic energy conversion.

2. Experimental

2.1. Hot Filament CVD

Boron doped diamond surfaces were grown using Hot Filament - Chemical Vapour Deposition techniques (HF-CVD). The diamond samples were grown by passing a mixture of gases through a vacuum chamber with hot wire filaments activating the gases. Inside the vacuum chamber, the three substrate disks lay close in distance (approximately 5 mm underneath) to 3 parallel tantalum wires that act as the hot filaments. When a base pressure of 1-2 mTorr had been achieved, the substrates were heated for 20 minutes at approximately 100 °C ($I = 4$ A) to allow any water to evaporate off the substrate disks. As Boron Doped Diamond (BDD) was required, the mixture of input gases was diborane (B_2H_6), methane (CH_4) and hydrogen (H_2), with CH_4 flowing at 1% of H_2 flow rate, and B_2H_6 flowing at a minimal flow rate compared to H_2 . The flow rates used are summarised in Table 6. The gas valves were opened and pressure stabilised at 20 Torr; the current was increased to 25 A, leading to a voltage of approximately 9 V and a filament temperature of at least 2000 °C. The current of the sample stage was increased to 6.75 A to heat the Si substrate to approximately 800 °C. The system was left to run for 3 hours, checking every 30 minutes that current, voltage, pressure and gas flow were all constant and the hot filament wires had not snapped. Figure 12 shows the schematic image of the HF CVD reactor used.

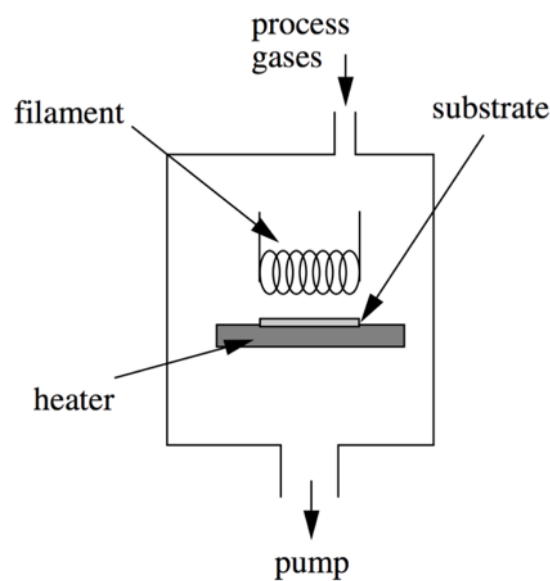


Figure 12: Schematic diagram of the HF-CVD reactor used for boron doped diamond growth [35].

Prior to use in the HF reactor, the substrates had to be seeded to provide nucleation sites [58]. Silicon substrates are soft enough that they can be manually abraded. This was achieved by taking two substrates and rubbing them together with 1-3 micron diamond powder between them.

Filament wire	Tantalum
Substrate	1 cm ² N-type silicon
H ₂ flow rate / sccm	200
CH ₄ flow rate / sccm	2
B ₂ H ₆ flow rate / sccm	0.005
Substrate temperature / °C	800
Chamber pressure / Torr	20
Current supplied / Amps	25
Time / hours	3

Table 6: Summary of the conditions used during the CVD boron doped diamond growth process.

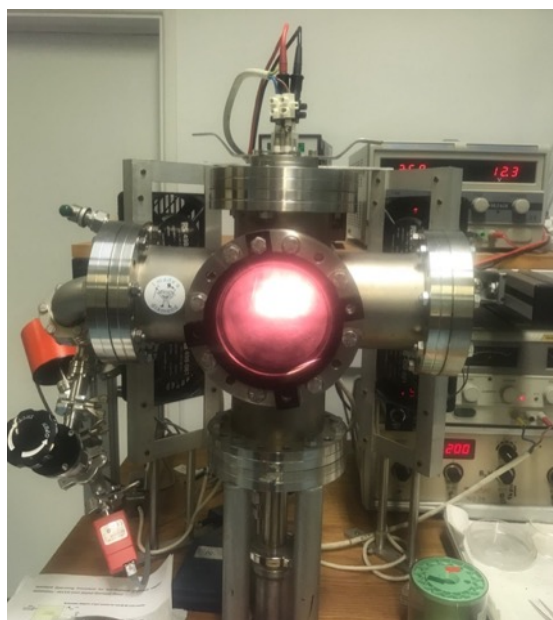


Figure 13: Hot Filament reactor used in the Bristol CVD Diamond Laboratory

2.2. Microwave Plasma CVD

Nitrogen doped diamond (NDD) surfaces were grown using an Applied Science and Technology, Inc. 'ASTEX-type' microwave plasma CVD reactor (as seen in Figures 14 and 15) [14]. The molybdenum substrate was positioned on top of a tungsten disk that lay on top of a thin Mo wired (4-8 ml) in the center of the heater (thickness of wire chosen is discussed later). When a base pressure of 0.03 Torr was achieved, the H₂ valve was opened. Pressure stabilised at 15 Torr. The plasma was struck at 675 Watts. Pressure was increased to 50 Torr where CH₄ and N₂ were introduced into the chamber. Power and pressure were slowly increased to 130 Torr and 1300 W, with the pressure being approximately 10% the value of the power. Reflected Watts were minimised to a maximum of 1 W by tuning with the tuning antenna. The time for growth was 15 minutes. The samples were cooled slowly by reducing the power by 100 W every 15 seconds. The pressure was reduced slowly so, again, it was

approximately 10% of the value of the power (i.e. a power of 1300 W would mean the pressure should be approximately 130 Torr). The conditions of growth are summarised in Table 7.

Prior to growth, the Mo substrates were seeded by placing the substrates in a solution of carboxyethylsilanetriol disodium salt in water for 5 minutes. The substrates were rinsed in deionised water multiple times before being placed in a nanodiamond suspension (18 nm diamond in water, 25 cts kg⁻¹) for 5 minutes. The substrates were washed again in deionised water and dried using a compressed air gun.

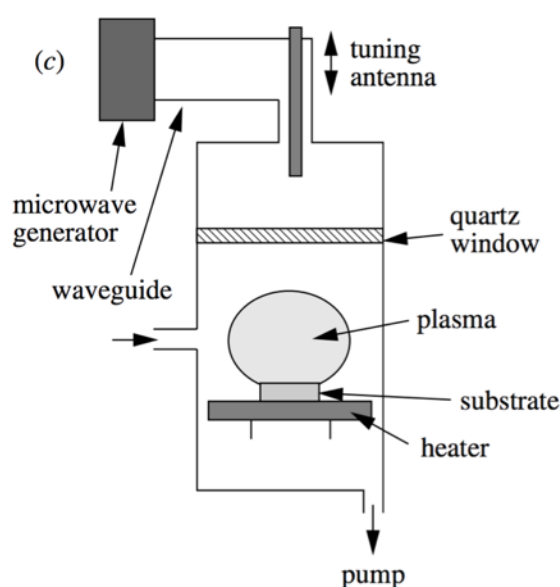


Figure 14: Schematic diagram of the microwave plasma reactor used during nitrogen doped diamond growth process. Taken from reference [14].

Substrate	1 cm ² molybdenum
H ₂ flow rate / sccm	300
CH ₄ flow rate / sccm	12.5
N ₂ flow rate / sccm	1.25
Chamber pressure / Torr	130
Chamber temperature / °C	850-900
Chamber Power / Watts	1300
Time / minutes	15

Table 7: Summary of the conditions used during the microwave plasma CVD nitrogen doped diamond growth process

2.3. Raman Spectroscopy

Renishaw 2000 laser Raman spectrometer was used to initially analyse the quality of the diamond films. The laser used is a focused beam of green light with a wavelength of 514 nm (Ar⁺). Raman spectroscopy was carried out on all samples to determine the quality of the diamond film by

comparing the sp^3 and sp^2 bond characterisation. The optical microscope attached to the Raman spectrometer was also used to visually assess the film quality.

2.4. Hydrogen Termination

The MW-CVD reactor was also used for hydrogen terminating the diamond samples. Hydrogen termination works similarly to initially growing the diamond using the microwave plasma reactor. A sample was placed in the reactor chamber on top of a tungsten disk with a 9mm wire in between the plate and substrate heater. The chamber was closed and allowed to reach a base pressure of approximately 0.03 Torr. Hydrogen flow was turned on, and the pressure stabilised at 15 Torr. The plasma striking power was set at 675 Watts. The plasma was struck with pressure and power being increased immediately, increasing at rates similar to each other so that the pressure value is 10% of the power value. Reflected Watts were minimised to a maximum of 1W.

When hydrogen terminating the diamond surface, there are three sequential regimes with varying conditions that take place. Regime 1) is at the highest pressure, power, and temperature of all three runs. The high temperature ensures the diamond surface is smooth and has been cleaned of any contaminants. Regime 2) has lower power, pressure, and temperature and is the stage where the hydrogen is deposited onto the surface. Regime 3) requires no power, which cools the sample down and ensures that a full surface termination of hydrogen has occurred. Table 8 summarises the standard conditions used in the Bristol CVD diamond laboratory for hydrogen termination of the diamond surface.

	Time of Regime / minutes	Power / Watts	Temperature / °C	Pressure / Torr	H ₂ Flow Rate / sccm
1)	2	1150	820	80	300
2)	2	650	500	30	300
3)	2	0	-	30	300

Table 8: Summary of conditions used to hydrogen terminate diamond surface using the microwave plasma reactor.

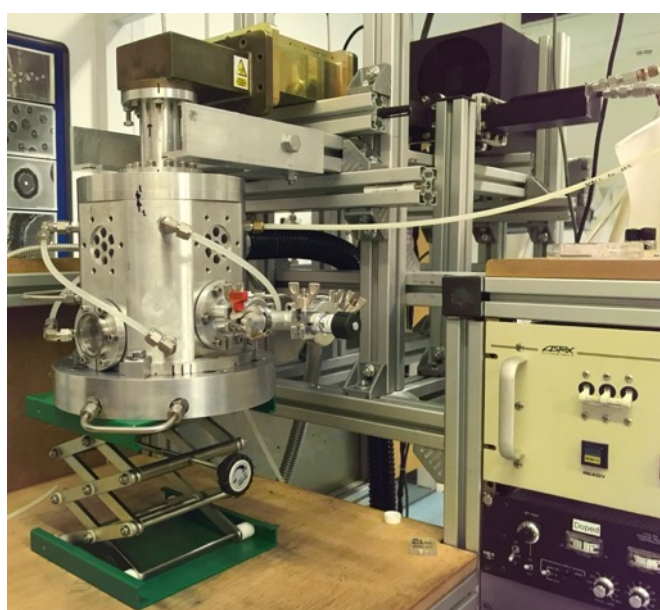


Figure 15: ASTEX-type Microwave Plasma reactor used to grow nitrogen doped diamond samples in the Bristol University CVD Diamond Laboratory.

2.5. Oxygen Termination

Samples were placed in the converted Edwards sputter coater (Figure 16) for oxygen termination of the diamond surface. A base pressure of 7×10^{-3} Torr was achieved before O_2 was introduced at a set flow rate of 10 sccm, allowing pressure to stabilise at 1 Torr. The HT voltage was set to 7 on a full-scale deflection of 10 in arbitrary units and kept constant; the O_2 plasma was initiated for 7 seconds

Conditions for oxygen termination:

O ₂ flow rate / sccm	10
Chamber pressure / Torr	1
Time / seconds	7
Voltage Dial / arb. units	7

Table 9: Summary of conditions used for oxygen termination



Figure 16: Converted Edwards sputter coater, nicknamed 'The Terminator', used for oxygen termination.

2.6. NanoESCA

The NanoESCA machine was used for surface analysis. The NanoESCA carries out all analysis techniques in ultrahigh vacuum (UHV), with a base pressure of 3×10^{-11} Torr and was used for X-ray Photoelectron Spectroscopy (XPS) and Ultraviolet Photoelectron Spectroscopy (UPS).

2.6.1. Annealing:

Prior to analysis by XPS and UPS, the samples were annealed for at least 30 minutes in UHV at 300 °C. This yields a clean surface ready for analysis by allowing atmospheric contaminants to desorb from the sample surface. The resistive heater used to heat the samples had a current of 2.44 A passed through it.

2.6.2. X-ray Photoelectron Spectroscopy

XPS is used to analyse the energy of the core electrons emitted. After annealing at 300 °C, a base pressure of at least 1×10^{-9} Torr was achieved prior to analysis. The samples were rotated to an angle of 85° relative to the analyser, to analyse the surface, rather than the bulk. An aluminium x-ray source was used, giving rise to x-rays with photons of 1486.70 eV of energy.

Two different XPS scans were taken for all samples analysed.

- 1) Survey: Repeated survey scans across the whole energy range to see what elements are present. Repeated scans to reduce background noise.
- 2) Core level scan To look at elements of interest, C 1s and O 1s. Again, repeated to reduce background noise.

X-ray Source	Aluminium target
Voltage Bias / kV	14
Filament Current / A	2.04
Emission Current / mA	17.8

Table 10: List of XPS conditions applied to nitrogen doped and boron doped diamond samples.

2.6.3. Ultraviolet Photoelectron Spectroscopy

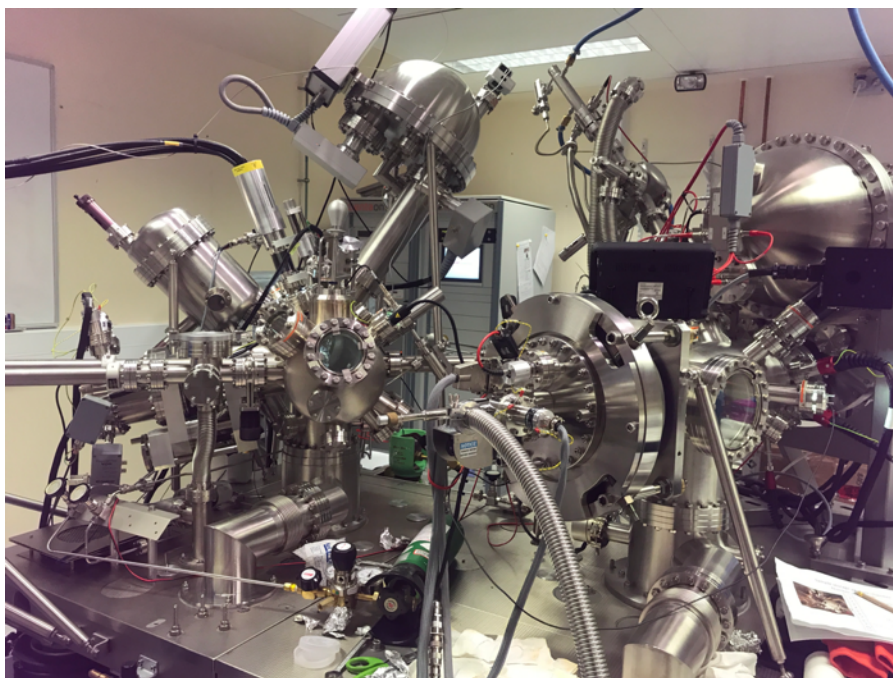


Figure 17: NanoESCA machine used for annealing, XPS and UPS analysis.

UPS was primarily used to determine the work function of the sample by taking a spectrum for each individual pixel. Hence, the surface work function can be determined by analysing the energy of the valence electrons emitted. UPS energy filtered analysis was run for samples B1-B3. A helium lamp was used to produce the high energy ultraviolet photons, the He I lamp emits photons with 21.2 eV of energy. The picture field of view was set at 78.1 μm . After the helium lamp is switched on, a pressure of at least 1×10^{-7} Torr was stabilised before UPS analysis was undertaken.

2.7. Sonication Cleaning

Prior to titanium deposition and scanning electron microscopy, the samples were cleaned using a sonication bath. Sonicating baths are successful in removing particles, such as dust particles, from the sample surface by using ultrasonic soundwaves to agitate the particles from the surface [42].

The samples were placed in a glass beaker with enough acetone to cover the sample. The glass beaker was placed in the sonicating bath and left to run for 5 minutes. The samples were then placed in a new beaker with the same amount of isopropyl and placed in the sonicating bath for another 5 minutes. The samples were dried using a compressed air gun.

2.8. Scanning Electron Microscopy

Scanning Electron Microscopy (SEM) was carried out on a range of samples to look at the quality of the samples and observe the difference between the NDD and BDD surface topographies. SEM images were taken on the JEOL JSM-IT300. Images of the detected secondary electrons were produced to provide topographic images of the sample.

The samples were placed on the stage and put in a vacuum. The working distance was set at 10 mm with a 15.0 kV voltage bias applied to accelerate the electrons.

Four images at different magnifications for each sample were taken. The chosen magnifications were x1000, x5000, x10,000 and x30,000. Each image at the different magnification was taken at a different position on the sample to stop electron beam damage affecting the quality of images.

2.9. Titanium Deposition

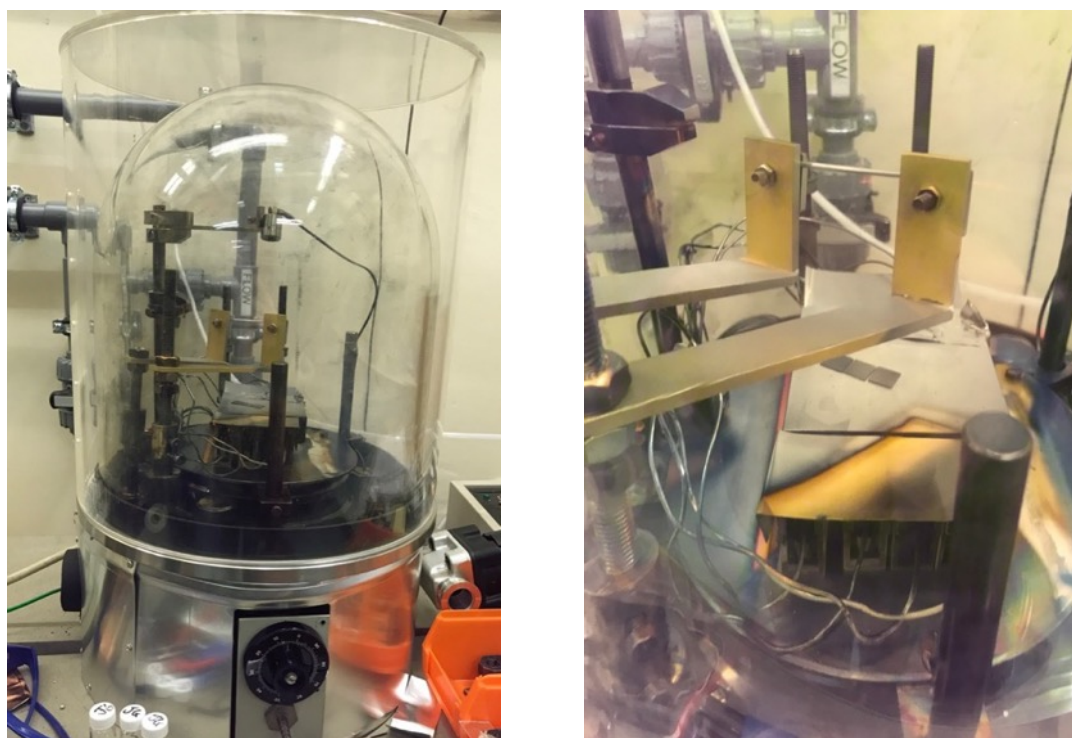


Figure 18: a) complete view of the Edwards bell jar evaporator used for titanium deposition and b) inside view of the titanium rod with substrates on the substrate heater.

Prior to titanium deposition, the samples were sonicated and then oxygen terminated using the methods above. The titanium rod was also sonicated to ensure a clean surface before use. A base pressure of at least 4.0×10^{-6} was reached. The sample stage temperature was set to 300 °C and left at

temperature for at least 30 minutes prior to Ti deposition to ensure a clean sample surface. Base pressure was attained again before deposition.

The Ti rod density is 4.506 g cm^{-3} , and so the Quartz Crystal Microbalance (QCM) was adjusted accordingly. The deposition rate of Ti was monitored using the QCM. As current increased, the temperature of the titanium rod was increased proportionally and the reading on the QCM increased as contaminants were degassed from the surface of the rod. The QCM reading was set back to 0 nm when the Ti rod started to glow orange and all contaminants had degassed. Once 0.1 nm of Ti had been deposited, the current was slowly reduced back to 0 and samples were cooled back to room temperature.

Titanium was deposited on another sample, under the same conditions as above but the sample stage temperature was set to $500 \text{ }^\circ\text{C}$, rather than $300 \text{ }^\circ\text{C}$.

2.10. Thermionic Electron Emission

Prior to thermionic emission testing, the Mo substrates were laser cut on the underside of the substrate to allow the sample to absorb the laser light, rather than reflect it. 1000 gratings of $10.6 \mu\text{m}$ wide were made across the sample.

The sample was put into the chamber and a pressure of approximately 2×10^{-6} Torr was reached. The temperature was measured using an optical pyrometer. A voltage bias of 25 V was applied. The temperature was increased by increasing the percentage of laser power.

The hydrogen terminated sample was heated for 3 minutes at $300 \text{ }^\circ\text{C}$ and then increased gradually to $750 \text{ }^\circ\text{C}$ where the temperature was kept steady for 3 minutes. The sample was cooled slowly to $300 \text{ }^\circ\text{C}$ where the laser was then switched off. For the titanium oxide terminated sample the conditions were kept the same, except that temperature was increased to $820 \text{ }^\circ\text{C}$, which is when the laser was at 100 % power.

3. Results and Discussion

3.1. Diamond growth

3.1.1. Hot Filament Reactor

Six boron doped diamond (BDD) samples were grown in the hot filament reactor by 2 runs of 3 samples each. The three substrate samples were aligned in a line underneath the tantalum wires. Both two runs ran successfully under the optimum conditions as stated in Section 2.1. Five of the six samples were very well grown and good to use for further testing, apart from sample B2 from Run 1. The silicon substrate was knocked from the correct position and so was not aligned directly under the tantalum wire. It is possible to see on the schematic below, Figure 19, how misaligning a substrate can considerably hinder the uniform growth of the diamond film. The temperature of the misaligned section will not be hot enough to promote even diamond growth across the substrate. After the samples were removed it was clearly visible without the need of an optical microscope to see the difference in the quality of growth of sample B2 when compared to samples B1 and B3. Sample B2 had patchy diamond growth towards the edge of the substrate that was not fully under the filament wires, whereas B1 and B3 had a uniform film across the whole substrate surface. There were no issues with samples B4 – B6.

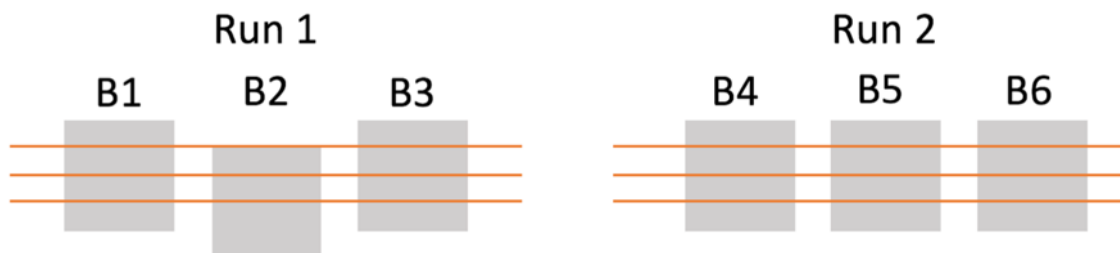


Figure 19: Schematic image of the two HF CVD growth runs with samples B1 – B6. The grey squares represent the silicon substrates and the orange lines represent the tantalum filament wires. Run 1 – sample B2 is misaligned underneath the filament wire and so growth was less uniform.

The flow rate of H_2 is significantly higher than the flow rate of CH_4 , flowing at 1% of the flow rate of H_2 . There are many reasons for such a high concentration of H_2 , but mainly due to the importance of atomic hydrogen during the CVD diamond growth process. Atomic hydrogen can quickly bond to the ‘dangling’ bond, keeping the sp^3 hybridised surface stable, preventing the rearrangement to sp^2 hybridised graphite. Diluting the precursor gas, CH_4 , in H_2 helps to promote the growth of diamond rather than other phases such as amorphous carbon or graphite. High concentrations of H_2 also helps to reduce the number of defects present in the diamond film by promoting good quality diamond growth. Atomic hydrogen also reacts with CH_4 , producing the required radical, CH_3 [14,36,37,50].

Tantalum wires were used for the filament wires as tantalum is as effective and cheaper than the other main alternatives, molybdenum and rhenium. Tantalum can withstand temperatures well above the necessary temperatures for growing diamond by HF-CVD. The tantalum filament is heated to temperatures of up $2200\text{ }^\circ\text{C}$ which dissociates hydrogen into atomic hydrogen; this occurs close to the filament as the gas temperatures are high enough to be dissociated. The filament wires can become brittle during the diamond growth as a tantalum carbide can form on the wires, after reacting with the methane in the process gases. This can alter the resistivity of the wires, becoming brittle and snapping during the diamond growth process, hence the need to check the wires are still intact every 30 minutes [14,36,58].

The substrate was heated to a temperature of approximately $800\text{ }^\circ\text{C}$ by applying a current of 6.75 A to the substrate heater. This ensures an even growth across the surface as it allows carbon atoms to

possess enough energy to move around the surface and, as a result, it promotes the growth of diamond rather than amorphous carbon [14].

3.1.2. Microwave Plasma Reactor

Twelve individual nitrogen doped diamond (NDD) samples were grown in the Microwave Plasma (MWP) reactor over two separate days. Table 11, below, summarises the qualities of the different growths. The sample quality was checked under an optical microscope and by Raman spectroscopy.

Sample	Quality of Growth	Temperature of Growth / °C	Wire Thickness / mm	Comments
N1	No diamond	1200	8	Sample not flat on tungsten disk.
N2	Patchy diamond	746 - 922	6	Temperature starts too low and finished too high.
N3	Good growth	805 - 970	6	Close to correct temperature range.
N4	Patchy diamond	965	6	Temperature too high.
N5	Patchy diamond	708 - 765	4	Temperature too low.
N6	Delaminated diamond	632	4	Delaminated on cool down.
N7	Good	784 - 869	6	Temperatures start slightly too low but quickly heat to correct temperature range.
N8	Good	766 - 875	6	
N9	Very good	803 - 862	6	
N10	Very good	846 - 895	6	
N11	Very good	849 - 899	6	
N12	No diamond	637 - 718	6	Temperature too low.

Table 11: Table summarising the quality of the diamond samples and the conditions affecting the quality. The samples highlighted in bold were good enough to be used for further testing.

When growing samples N1 – N6, there was a problem with the reactor power supply giving rise to a large temperature range. The optimum temperature for diamond growth in the MWP reactor is 850-900 °C. As seen in Table 11, only N3 diamond has grown well, as the majority of growth time was in the correct range. The temperature for growth of N1 was far too high as the sample was not flat on the tungsten disk. There was a protective layer still partly stuck on the molybdenum substrate which caused the substrate to lie at an angle rather than flat on the disk, and so the temperature of the substrate was far too high. Samples N2-N4 were grown using a 6 mm wire, instead of 8 mm with N1. Using a thinner wire lowers the temperature of the substrate as the substrate lies closer to the water cooler. A 4 mm wire was used for samples N5 and N6 to try to decrease the temperature of growth, but the lowered temperature meant that diamond growth was either poorly grown or not possible. N6 was cooled too quickly and so that meant the diamond film had delaminated off the Mo substrate. This was evident as the film had a rippled and shiny effect rather than a smooth rainbow effect that should be present if the diamond film had not delaminated.

Once the power supply was fixed, six more samples were grown, N7 – N12. 6mm wires were used for every run which made the substrate temperature lie in the correct temperate range for all samples except N12. N12 diamond growth was very poor as the temperature was far too low. This could be due to human or technical errors, such as dust making the substrate not lie flat on the tungsten disk or the plasma ball was not positioned correctly above the substrate. This sample was discarded. Samples N9 – N11 had successful growths.

The samples were cooled slowly by reducing the power by 100 W every 15 seconds. The pressure was reduced slowly so it was approximately 10% of the value of the power. Diamond and molybdenum have different thermal expansion coefficients; diamond has a much lower thermal expansion coefficient than Mo, meaning that when heated, Mo expands more than diamond. When the sample is cooled, the Mo substrate has to contract much more than diamond. Delamination of the diamond film occurs when the diamond film and Mo substrate have cooled down too fast and so the diamond film separates from the substrate due to the difference in thermal expansion coefficients. In order to prevent separation from happening the power was reduced slowly to encourage slow contraction of the substrate upon cooling [40].

3.1.3. Comparing Hot Filament CVD against Microwave Plasma CVD

Atomic hydrogen is required for both HF-CVD and MWP-CVD, but instead of thermal activation of the gases in HF-CVD, atomic hydrogen is made by electron impact on H₂ in MWP-CVD. The microwaves enter the vacuum chamber by passing through the quartz window which creates an electric discharge. The high energy electrons collide with the gas particles, transferring energy that in turn makes the gas particles dissociate, which is required for CVD diamond growth [4,14].

The CVD growth process time was significantly shorter when using the MWP reactor than when using the HF reactor; 15 minutes and 3 hours, respectively. As stated in the literature, NDD grown in the MWP reactor has a growth rate of up to 16 μh^{-1} and BDD grown in the HF reactor typically has a growth rate of approximately 1 μh^{-1} [61-64]. The increased growth rate of the MWP reactor is due to the electric discharge activating the gases more successfully than by thermally activating them in the HF reactor [14,36], hence growth rate for MWP-CVD is much faster than HF-CVD. The growth times for the differently doped diamonds correspond to similar growth thickness of approximately 3 μ .

Even though the MWP reactor growth rate is significantly faster, the HF reactor was used for BDD rather than the MWP reactor as boron sticks to the chamber sides and is difficult to remove after use. This would contaminate any further non-BDD grown in the MWP reactor with boron, and so BDD has a separate HF reactor where only BDD is grown as HF reactors are much cheaper to purchase and run compared to MWP reactors.

Another advantage of using MWP reactors as opposed to other CVD techniques is that in the MWP reactor the electric discharge is produced without the need for electrodes. This stops the risk of contamination of the electrode into the diamond film [41].

The samples grown in both the HF and CVD reactors were grown on carbide-forming substrates, Si and Mo, as the rate of growth on a carbide-forming substrate is several times higher than the rate of growth on a non-carbide forming substrate, such as Cu. This is due to the carbide formation helping the initial nucleation of diamond to begin [44].

3.2. Raman Spectroscopy

All samples, B1 – B6 and N1 – N12, were tested via Raman spectroscopy and the optical microscope attached to ensure the visual predictions were correct. The Raman spectrometer is a useful characterisation tool as it allows the sp² and sp³ content of the samples to be evaluated.

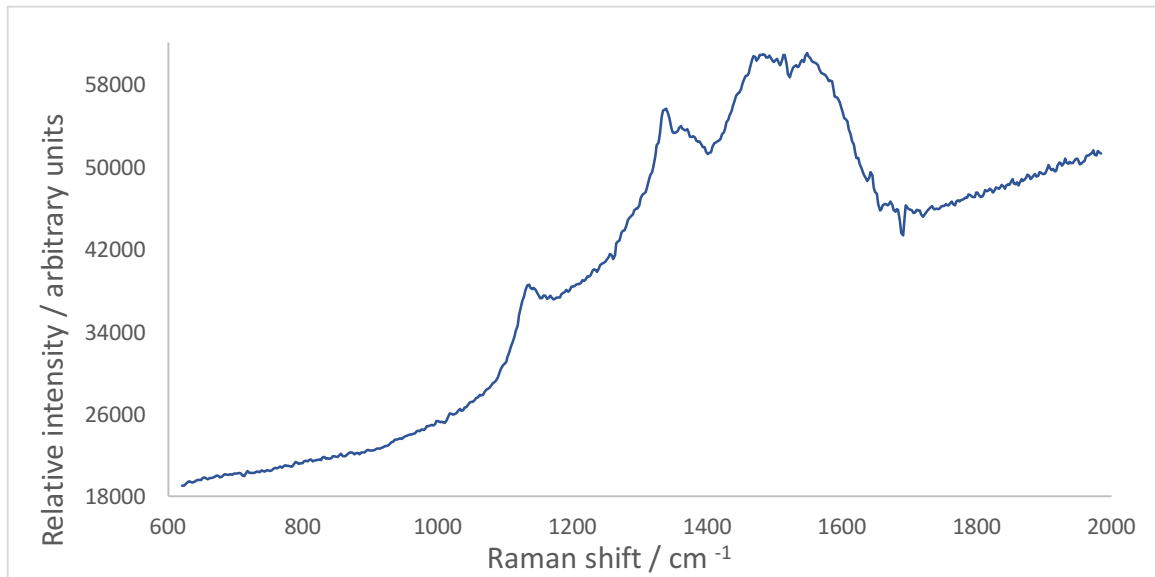


Figure 20: Raman spectrum for N10, taken on the Renishaw 2000 laser Raman spectrometer.

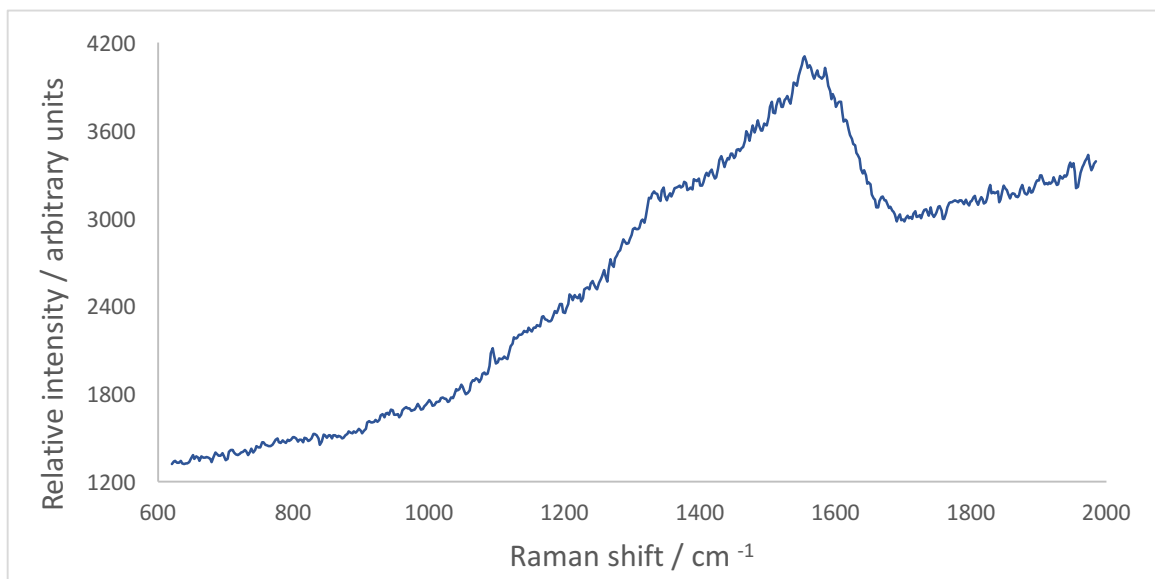


Figure 21: Raman spectrum for N12, taken on the Renishaw 2000 laser Raman spectrometer.

N10 spectrum (Figure 20) is similar to the other correctly synthesised NDD and so N10 was picked to show the difference between a good and poor growth NDD Raman spectrum. The diamond growth and quality of N12 is much poorer than for N10. The difference in quality between the two diamond films is obvious from looking at the Raman spectra. The relative intensity is much lower for N12 (1200-4200) than it is for N10 (18000-58000). The literature value for the characteristic sp^3 peak in nanocrystalline diamond is at 1332 cm^{-1} but is shifted to a slightly higher wavenumber when nitrogen doped due to the shortened bond length.

For NDD, the peak shifts slightly as seen in N10 where the peak lies at 1334 cm^{-1} , but for N12 where diamond growth was very poor, there is a small peak at 1332 cm^{-1} . This shows that barely any diamond had grown as the peak is so small and little nitrogen was incorporated into the film as the peak had not been shifted to a higher wavenumber. There is also more background noise affecting the spectrum for N12 as the relative intensities are much lower. The sloping background is due to the

photoluminescence of the sample [48]. The N10 peaks at 1135 and 1478 cm^{-1} are due to transpolyacetylene formation at the grain boundaries [48,49]. The small peak at 1346 cm^{-1} and the larger peak at 1548 cm^{-1} are due to the sp^2 amorphous carbon, D and G peaks, respectively [48,51,52].

The optical microscope attached also helped to show the difference in the quality of the two samples, as seen in Figure 22. The images of N6 (Figure 23) and N7 were also included as it is very clear to see the difference between the correctly grown samples, N10 and N7, compared to the poorly grown samples, N6 and N12.

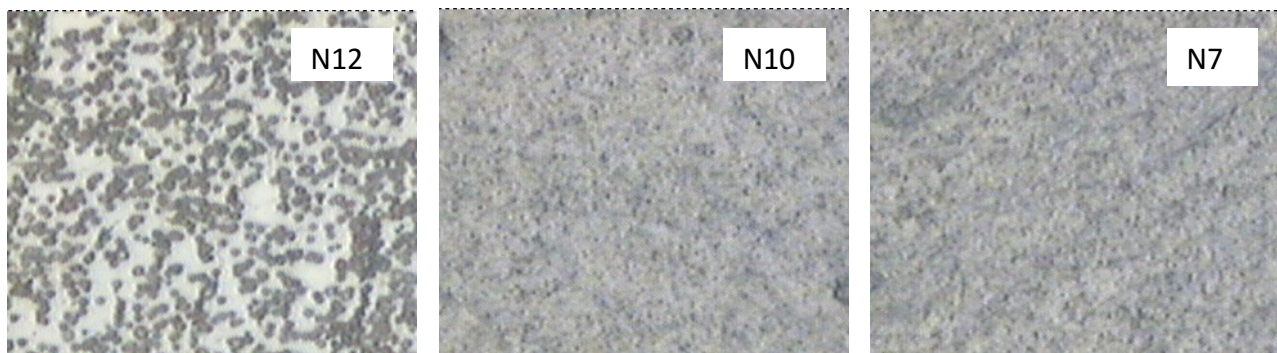


Figure 22: Optical microscope images to help assess the quality of the diamond growth. N12 shows a poor growth where temperature was too low. N10 and N7 show good growths.



Figure 23: Optical microscope image of N6 diamond film which delaminated from the Mo substrate, shown by the rainbow effect.

As seen in the Raman spectrum for B2 (Figure 24), the growth of diamond is better than originally thought when compared to the spectrum for B3 (Figure 25). The characteristic diamond peak at 1332 cm^{-1} has been downshifted in energy to 1317 cm^{-1} and 1320 cm^{-1} for B2 and B3. The more a peak is downshifted in energy corresponds to an increase in the concentration of boron incorporated into the diamond film [53]. A small difference of only 3 eV could just be down to the slightly different growths, with B2 being slightly misaligned under the filament wires. The asymmetric Fano line shape at 1220 cm^{-1} is due to boron doping [53]. Both spectra show a weak, broad peak at approximately 980 cm^{-1} corresponding to second-order scattering from the Si substrate [55]. The large, sloping background is due to photoluminescence or incorporation of Si from the substrate into the sample [48,54]. Figure 26 shows the uniform growth of B3, which is expected for correctly grown diamond surfaces.

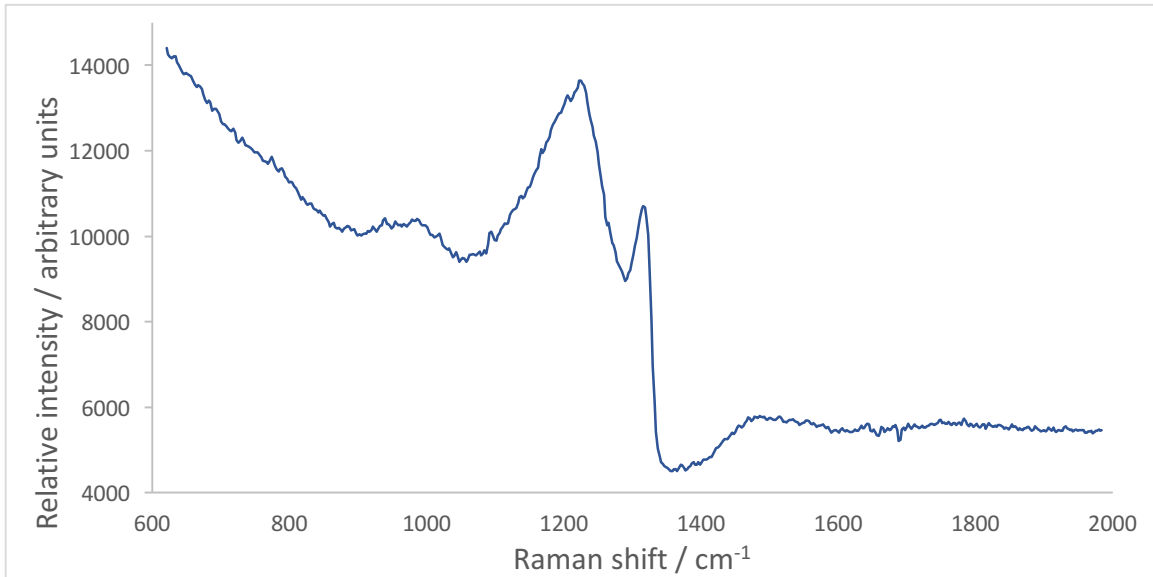


Figure 24: Raman spectrum for B2, taken on the Renishaw 2000 laser Raman spectrometer.

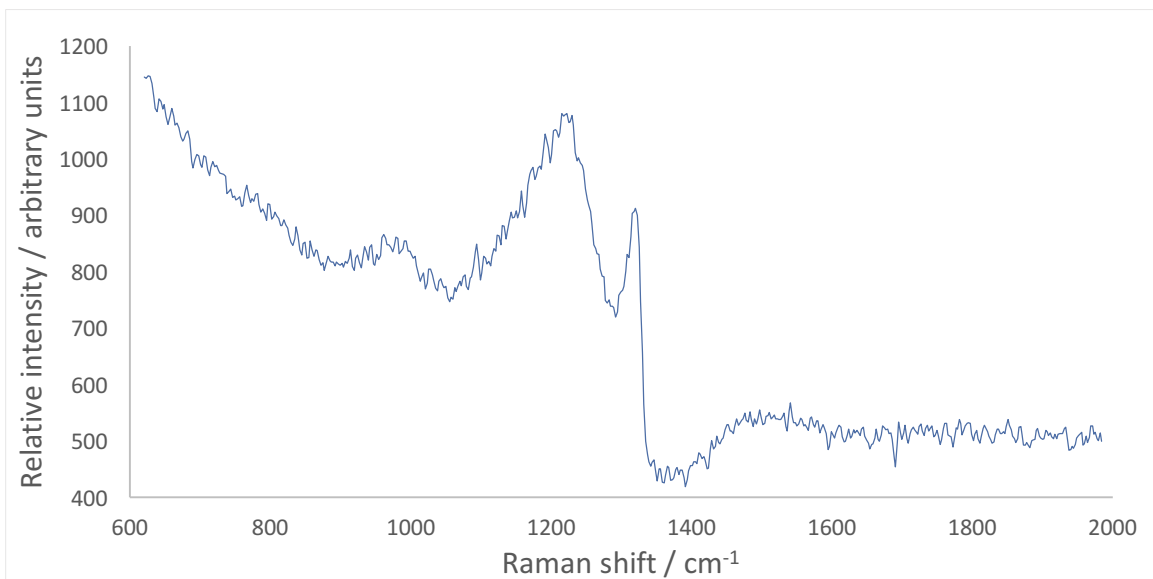


Figure 25: Raman spectrum for B3, taken on the Renishaw 2000 laser Raman spectrometer.



Figure 26: Optical microscope image taken of samples B3.

3.3. Hydrogen Termination

Over time, oxygen will displace hydrogen from the surface of diamond, and so when analysing a hydrogen terminated surface the termination must be completed and immediately followed by the necessary analysis. This allows the vast majority of the surface to still be hydrogen terminated.

Several hydrogen terminations were completed throughout the course of the project. All terminations ran as expected under the required conditions except the first hydrogen termination where the reactor power supply was not running correctly. Table 12 summarises the conditions of the termination with the faulty power supply. Regime 1 was allowed to run for 30 seconds to see if temperature stabilised to a slightly lower temperature than was originally shown. The temperature did not reduce after 30 seconds so power was reduced from 1150 W to 1017 W. Pressure was also reduced from 82 Torr to 72 Torr. Modifying the power and pressure helped to reduce the temperature so it was slightly closer to the optimum hydrogen termination temperatures. Regime 1 was then corrected and allowed to run for the allotted 2 minutes. Regime 2 was also operated at a lower power than stated above as temperature was, again, slightly too high.

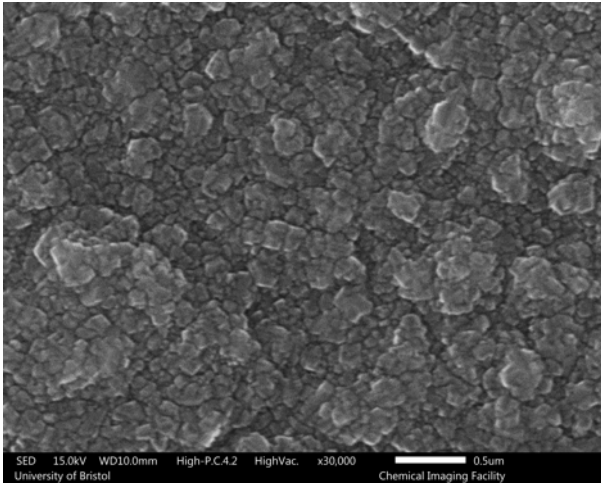
Once the power supply was fixed, all hydrogen terminations ran smoothly at the required conditions, giving rise to a temperature of within 20°C of the optimum hydrogen termination temperatures.

Regime	Time of Regime/ minutes	Power / Watts	Temperature / °C	Pressure / Torr	H ₂ Flow Rate / sccm
1	0.5	1150	998	81.7	300
Corrected 1	2	1017	910	72.0	300
2	2	605	560	31.0	300
3	2	-	0	31.0	300

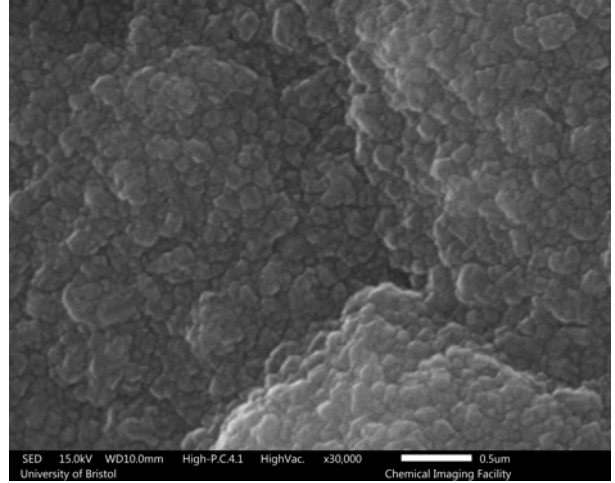
Table 12: Summary of hydrogen termination with faulty power supply. Powers and pressures were modified to achieve a temperature close to optimum hydrogen termination temperatures as stated in the experimental section above.

3.4. Scanning Electron Microscopy

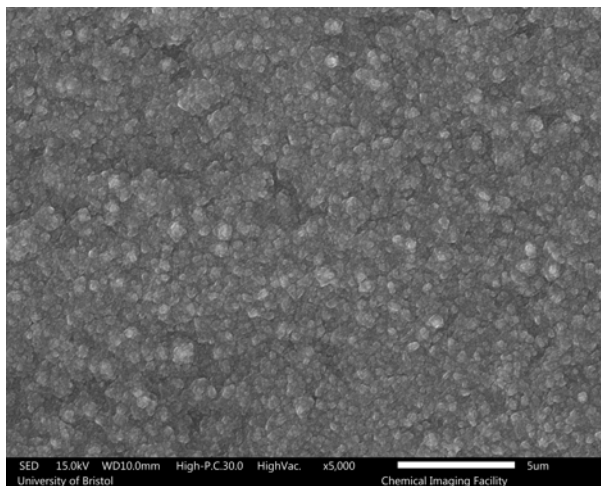
Images of samples B4, B6, N2, N6, N7, N9, and N11 were taken using the Scanning Electron Microscope (SEM). All samples had 4 different magnifications chosen: x1000, x5000, x10,000, x30,000, with only images of interest displayed for discussion. When comparing samples N7 and N11, it is obvious N7 has a more uniform surface with evenly sized smaller crystal growths, whereas N11 has some larger growth facets, some of which are up to 5 µm in size (as seen in Figure 27). N7 looks to be more like nanocrystalline growths as the facets are smaller than 500 nm, with N11 having some microcrystalline diamond clusters [56]. The temperature for the growth of N11 was slightly higher than for N7. Renucleation is more dominant in higher temperatures as increased hydrogen dissociation occurs, increasing the concentration of carbon radicals and hence, increasing the rate of renucleation and cross-linkage [60].



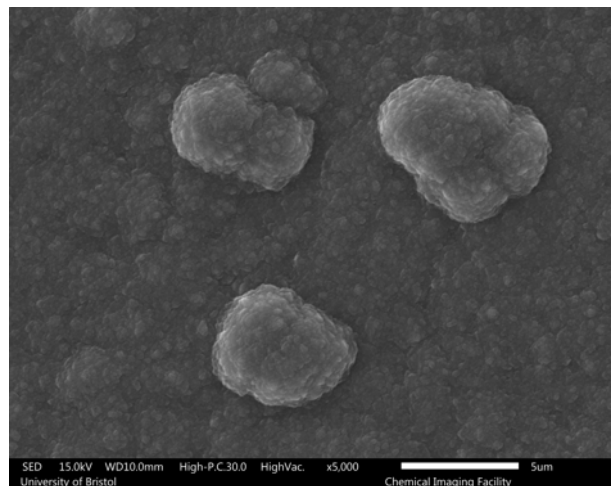
N7 x30,000



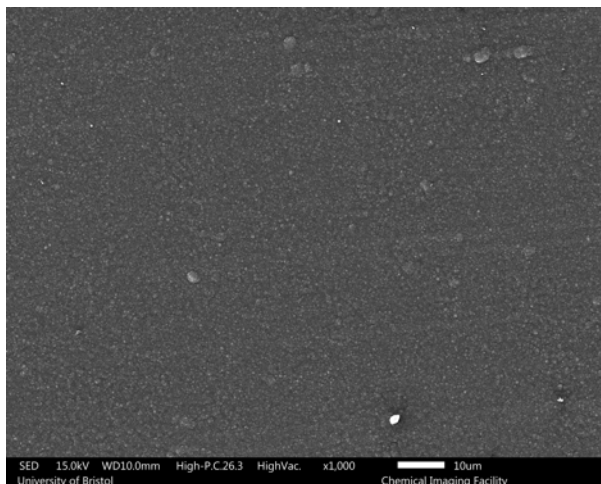
N11 x30,000



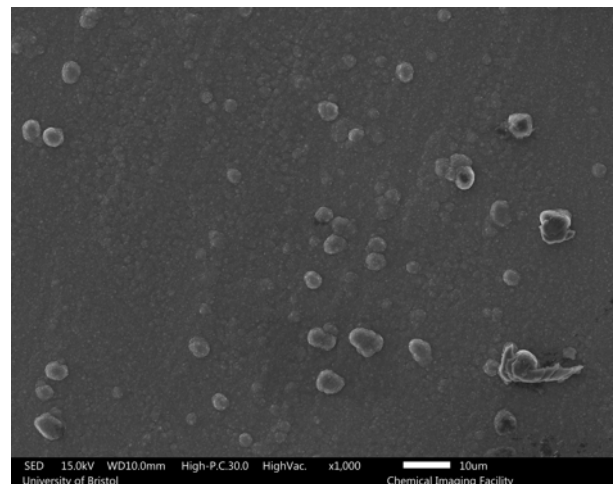
N7 x5,000



N11 x5,000



N7 x1,000



N11 x1,000

Figure 27: SEM images taken from samples N7 and N11 at the different magnifications.

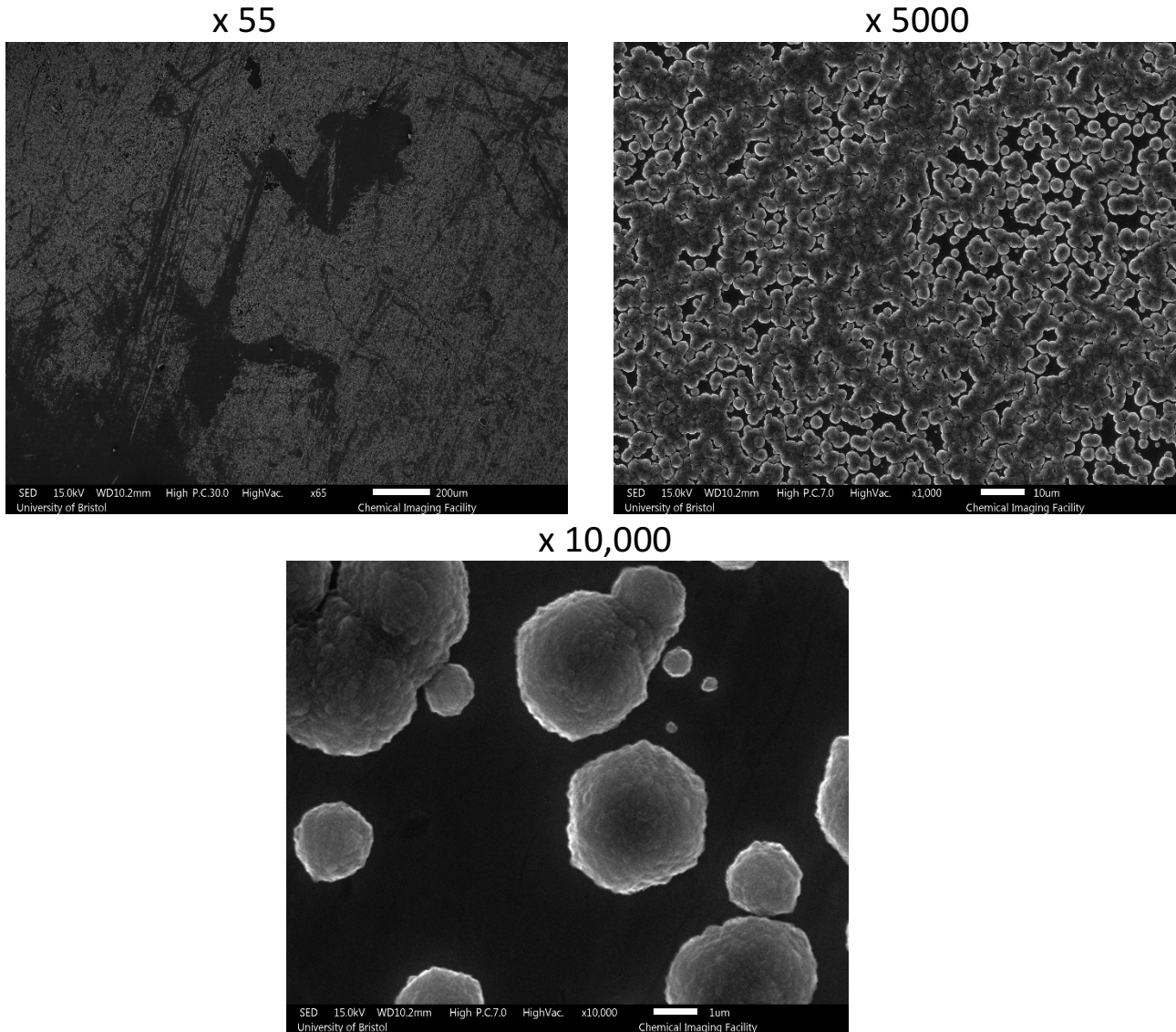


Figure 28: SEM images taken of poorly grown N2. Magnifications of x55, x5000, x1000

Figure 28 shows the SEM images for N2. The diamond growth for N2 started off over 100 °C lower than the optimum NDD growth conditions. The temperature did eventually rise, but the majority of the growth time was when the temperature was too low, inhibiting the growth of diamond. The black background on the SEM images is the molybdenum substrate when no diamond has grown.

Figure 29 shows the SEM images for B4 with magnifications of x1000, x5000 and x10,000. There is an even surface coverage with some larger crystals of up to 5 µm in size. The Si substrate was initially seeded by rubbing two substrates together with diamond dust in between the substrates. The larger crystals could be from more successful seeding that leads to the initial growth rate being faster in those areas, and as a result, produces larger crystals in certain patches.

The appearance of the different BDD and NDD facets stems from the ratio of [CH₄] to [H₂] during growth. The more rounded facets of MWP-grown NDD is due to the relatively high concentration of CH₄ compared to the HF-grown BDD CH₄ concentration. As the concentration of radical carbon increases, the ease of atomic hydrogen terminating the 'dangling bond' decreases, meaning that cross-linkage between the surface carbon atoms is more likely. As a result, the NDD film has a

smoother appearance with smaller crystals, but with higher graphitic impurities; BDD has sharper crystal edges [60].

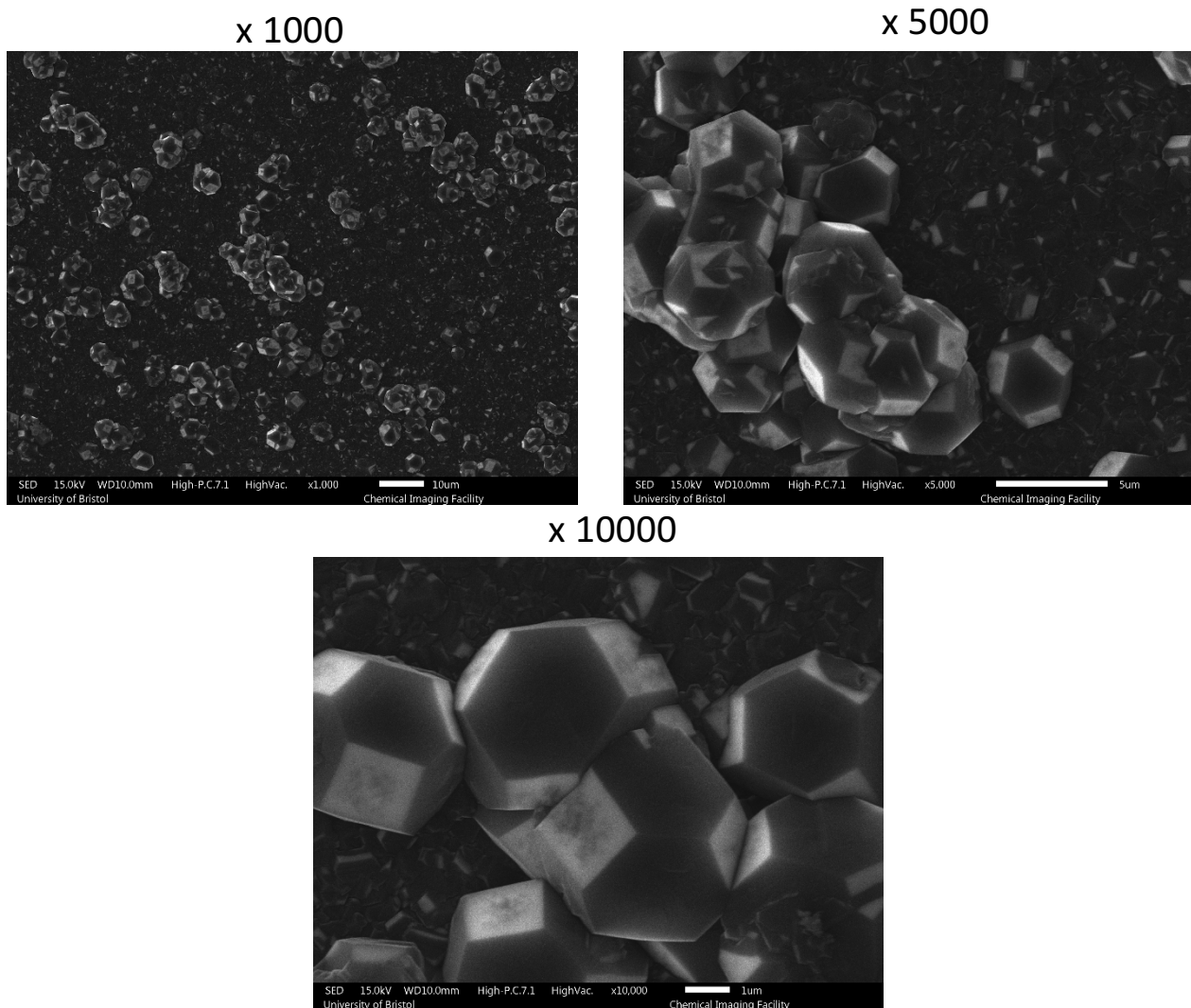


Figure 29: SEM images of B4. Magnifications of x1000, x5000, x10,000

3.5. Bell Jar Evaporator

At the beginning of the project, it was hoped a new metal deposition chamber on the NanoESCA would be ready to use to deposit titanium onto oxygen terminated diamond. Unfortunately, close to the end of the project it still wasn't ready in time so the Edwards bell jar evaporator was used instead.

It proved difficult to tell if titanium had been deposited or if it was contaminants desorbing from the Ti rod and sample surface when using the QCM. The smallest measurement the QCM recorded was 0.1 nm which is 1 Å, so it was hard to be precise when seeing how much titanium had been deposited. This meant it was hard to achieve the required monolayer coverage. In order to make sure it was Ti deposition making the QCM reading increase, the sample stage was heated to 300 °C and current was increased slowly to try to degas any contaminants prior to titanium deposition. After analysis via XPS (discussed below), it was noted that no Ti had been deposited and so when depositing Ti on the next sample, the sample stage was heated to 500 °C. Unfortunately, the filament blew when the stage was approximately 450 °C, and so could no longer be used. Due to time constraints on the project, there was insufficient time for the filament to be repaired and the titanium deposition process repeated.

3.6. X-ray Photoelectron Spectroscopy

XPS is one of the key solid surface analysis techniques used on the NanoESCA machine. XPS can determine almost all surface elements except H and He [43]. XPS works by heating a filament which releases electrons, these electrons are accelerated by a large voltage bias. The accelerated electrons hit an aluminium plate that then releases high energy X-rays. These high energy X-rays hit the diamond sample being analysed and excite core electrons from the sample that are detected by the detector. The detector measures the kinetic energy of the core electrons. The current and voltage applied were kept the same for all samples tested to ensure the aluminium x-rays had the same energy.

Five samples were analysed by XPS. Table 13 lists the surface terminations of the five samples.

Sample	Surface Termination
B1	Oxygen
B2	Oxygen
B3	Hydrogen
B4	Titanium oxide
N9	Titanium oxide

Table 13: The different samples analysed by XPS and their respective surface terminations.

The data for the Ti-O terminated samples, B4 and N9, showed no peak for Ti and so it was determined no Ti was initially deposited using the bell jar evaporator. The NDD sample proved difficult to measure the binding energies via XPS as NDD has a deep donor level of 1.7 eV below the conduction band minimum and so NDD samples are not conducting at room temperature [11]. Due to the positive charge accumulating on the surface, the binding energy for C 1s was shifted from 285 eV to 287 eV. N9 sample was heated to 300 °C to try to get the sample to conduct electricity, but even at an elevated temperature, the binding energy was still shifted to 287 eV.

Name		B1		B2	
		Position (eV)	% Area	Position (eV)	% Area
C 1s	sp ²	282.7	2.18	282.9	4.70
	sp ³	284.5	82.43	284.6	74.86
	C-O or C-O-C	285.8	13.24	285.7	15.88
	C=O	286.9	2.14	287.2	4.56
O 1s	Ketone	532.5	94.91	532.5	94.11
	Ether	534.6	5.09	533.9	5.89

Table 14: XPS data for B1 and B2, showing the binding energies for the various C 1s and O 1s peaks, with the individual compositions of bonding.

The two oxygen terminated samples, B1 and B2, yield very similar results, as seen in Table 14. The C 1s sp³ content for B1 is slightly higher than for B2. This is because B2 was slightly misaligned under the filament wires, and so part of the substrate was at a temperature slightly too low for optimum diamond growth. High temperatures are required to promote sp³ diamond growth, rather than sp² graphite or amorphous carbon [14]. The O 1s percentage area coverages are approximately equal for B1 and B2. The oxygen terminations were carried out under exactly the same conditions, with both O-terminated samples being annealed at 300 °C prior to XPS analysis. The binding energy for ketone or ether bonded oxygen is very similar (as discussed in Section 1.3.2.), and so different oxygen termination procedures favour different bonding configurations. Ether bonding is primarily seen when wet oxidation techniques are used and ketone bonding is normally seen when dry oxidation techniques are used. Samples B1 and B2 were oxygen terminated using dry O₂ plasma, hence mostly ketone bonding is visible. As the ketone and ether bonding configurations lie very close in energy,

some ether bonding is present, but it is mostly ketone bonding due to the oxygenation technique used [57].

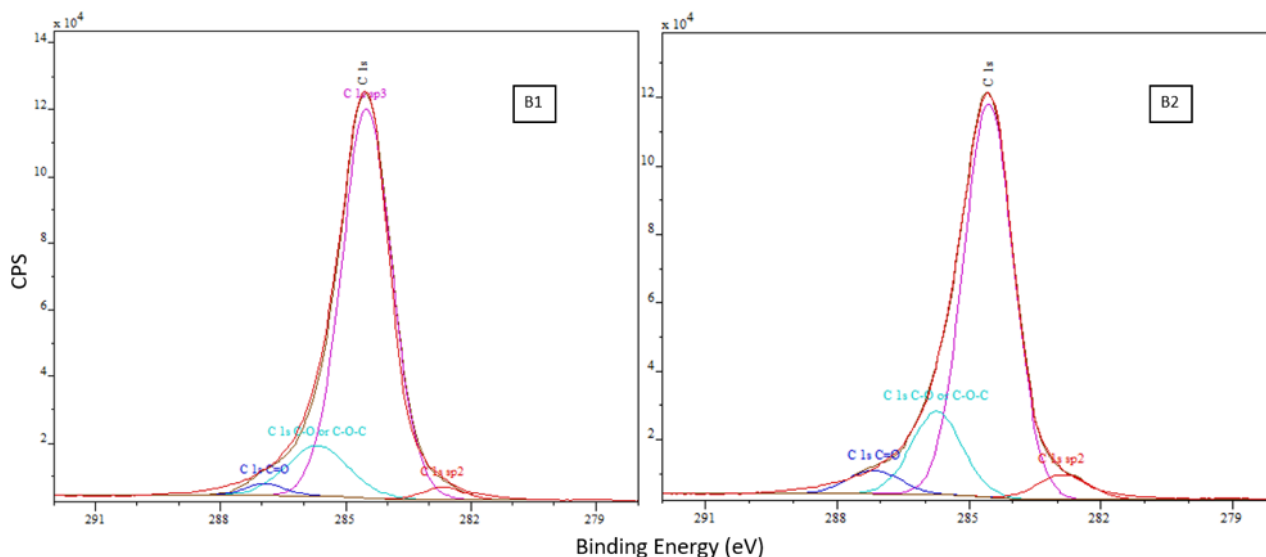


Figure 30: CasaXPS analysed data for C 1s peaks for B1 and B2.

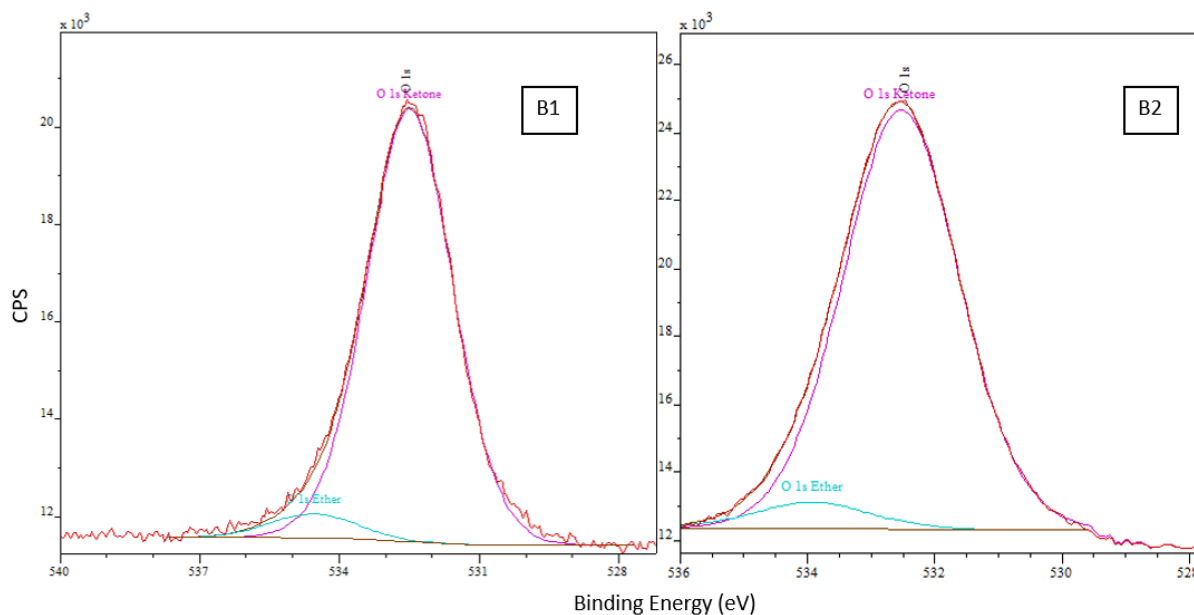


Figure 31: CasaXPS analysed data for O 1s peaks for B1 and B2.

Figures 30 and 31 show the XPS spectra for samples B1 and B2, showing the relative binding configurations corresponding to both samples. As seen in Figure 30, the sp^3 configuration dominates for the C 1s spectra, and in Figure 31 the ketone configuration dominates for the O 1s spectra.

B3	Name	Position (eV)	% Area
C 1s	sp^2	282.8	5.31
	sp^3	284.5	89.84
	C-O or C-O-C	285.9	2.78
	C=O	286.6	2.07

Table 15: XPS data for C 1s peak for B3.

Table 15 summarises the XPS data for B3 C 1s peak. B3 had very similar conditions of growth to B1 and so relative percentage of sp^3 bonded C is the highest, showing good diamond growth. Figure 32 shows there is a slight O 1s peak for B3 as hydrogen terminated diamond is slowly naturally oxidised, replacing the hydrogen with oxygen over time. In order to minimise the rate of oxidation the sample was placed in UHV as quickly as possible.

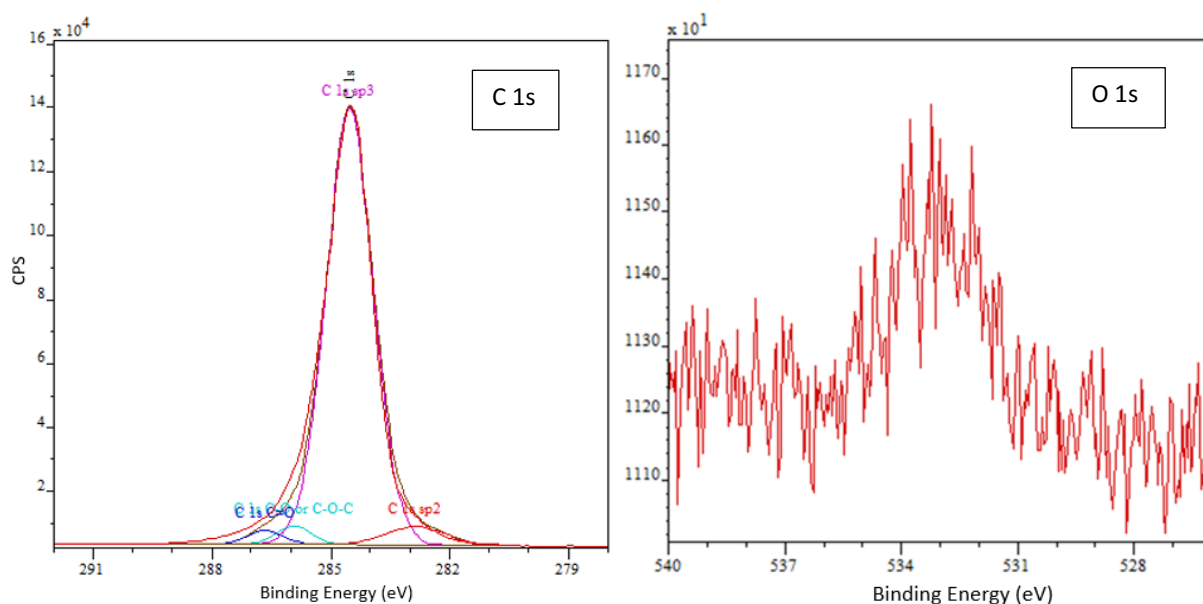


Figure 32: CasaXPS spectra of C 1s and O 1s peaks for sample B3.

A survey spectrum for each sample was carried out, showing the relative composition of the top few layers of atoms, as shown in Table 16. The percentage area of O:C is slightly lower for B2 compared to B1 which could be down to the slight increase in C-O/C-O-C bonding as in the C-O-C bonding each oxygen is bonded to two carbon atoms, reducing the percentage of oxygen on the diamond surface. Figure 33 shows the survey spectrum for B1, which is similar to the survey spectrum for B2. Figure 33 shows the O KLL Auger peak at approximately 975 eV and the secondary carbon peak at approximately 320 eV.

	Name	Position (eV)	% Area
B1	O 1s	533.0	4.24
	C 1s	285.0	95.76
B2	O 1s	532.5	2.62
	C 1s	284.5	97.38
B3	O 1s	534.0	0.04
	C 1s	284.5	99.96

Table 16: CasaXPS data of survey for samples B1-B3, showing the different compositions of oxygen and carbon.

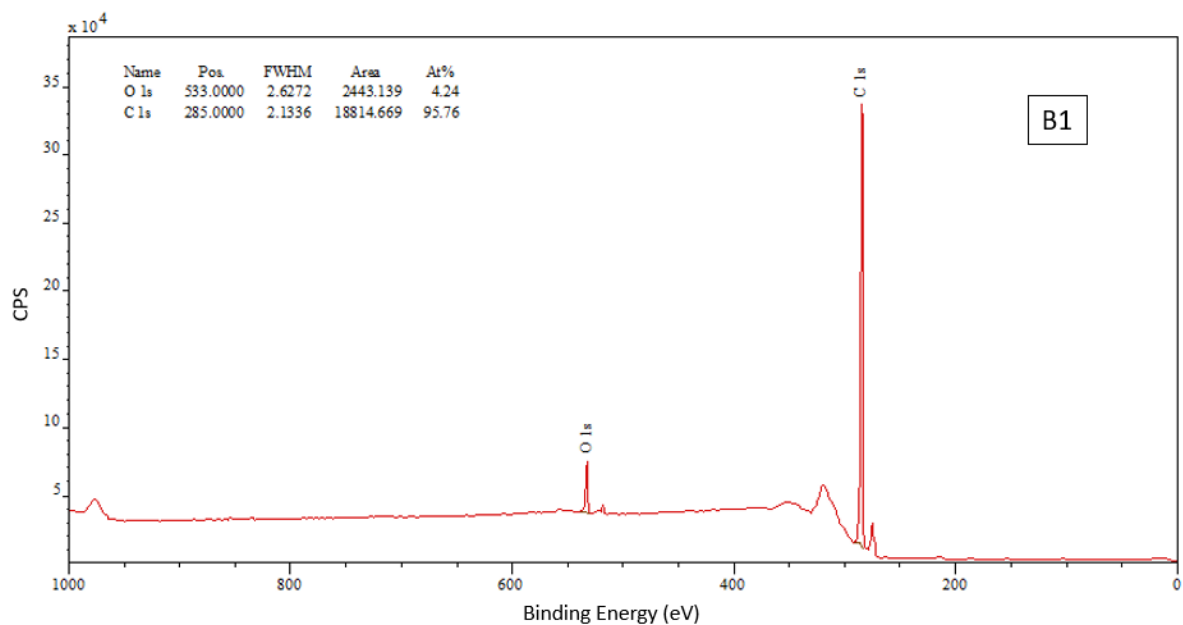


Figure 33: CasaXPS survey spectrum for sample B1, showing the different peaks.

3.7. Ultra-violet Photoelectron Spectroscopy

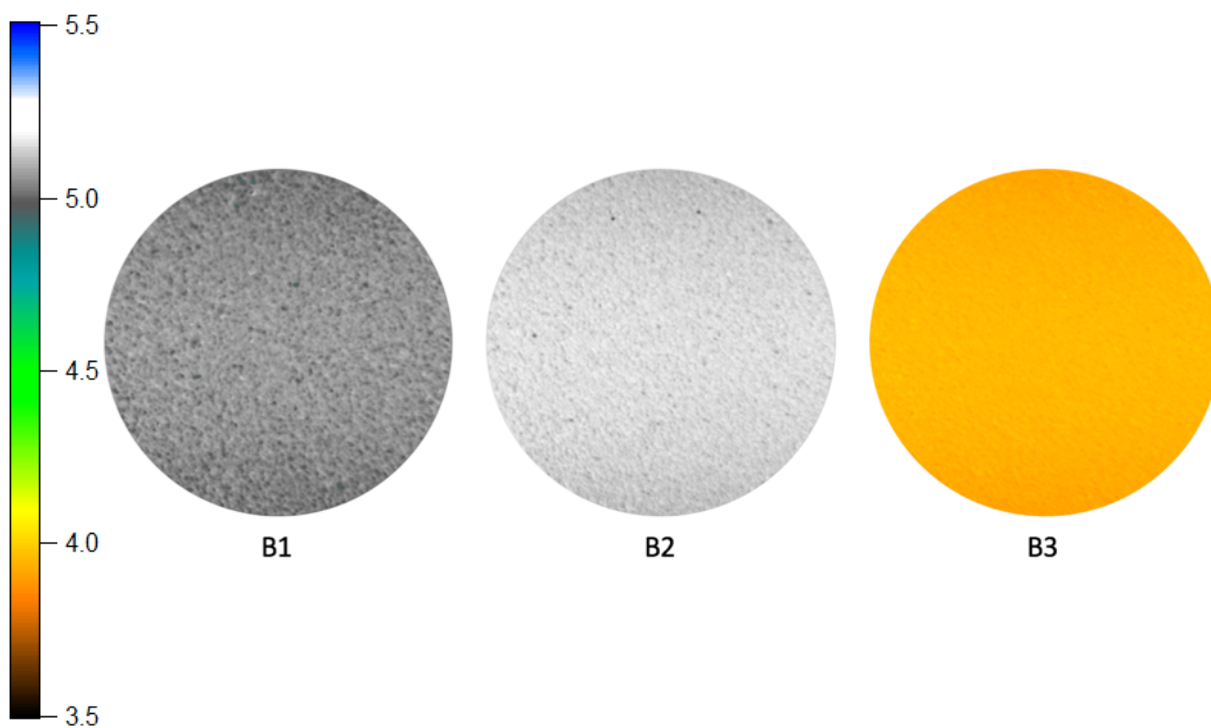


Figure 34: Energy-filtered UPS work function map for samples B1-B3 with colour scale bar showing different work functions.

Energy-filtered UPS was carried out on samples B1-B3, compiling images over different energies for each pixel to produce a work function map for each sample. Table 19 states the different surface termination for each sample and the sample's respective work function. The field of view for all three samples was kept constant, being $78.1 \mu\text{m}$.

As discussed in Section 1.3., oxygen termination on diamond surfaces induces a PEA, along with hydrogen termination inducing an NEA. This is evident in the experimental results from the work function mapping as the hydrogen terminated sample has a work function over 1 eV lower than the oxygen terminated samples. Samples B1 and B2 were both oxygen terminated, yielding a work function of approximately 5.10 eV. The very small difference in work function between the two oxygen terminated samples is just due to slight variations between the diamond films, such as grain boundaries. The experimental results are summed up in Table 17.

	Termination	Average Work Function (eV)
B1	Oxygen	5.05
B2	Oxygen	5.15
B3	Hydrogen	3.95

Table 17: Summary of average surface work function for samples B1-B3 and their respective surface terminations.

The energy-filtered UPS system can have a sensitivity of up to 20 meV, hence producing a very accurate image [59]. All three films show a uniform colour across the surface, which shows the growth and terminations were even over the section of the surface analysed, as shown in Figure 34.

3.8. Thermionic Electron Emission

Thermionic electron emission was tested for N4 and N9. N9 was supposedly titanium oxide terminated, but as discovered via XPS, no titanium had been deposited onto the surface. N4 was hydrogen terminated. Figures 35 and 36 show how thermionic current varied with respect to temperature for samples N4 and N9.

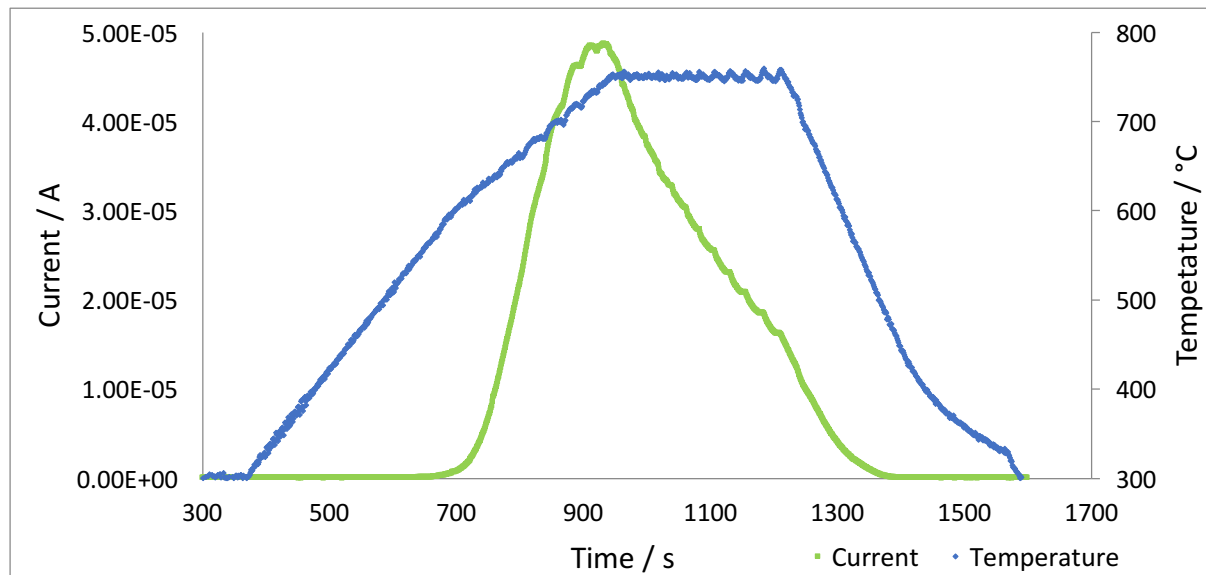


Figure 35: Thermionic electron emission for H terminated N4

Using the Richardson-Dushman equation, the work function for the hydrogen terminated N4 sample was determined.

The Richardson-Dushman goes as follows: $J_e = A_G T^2 e^{-\phi/k_B T}$

Where: J_e is thermionic current density ($A m^{-2}$), A_G is Richardson-Dushman constant ($A m^{-2} K^{-2}$), T is the absolute temperature of emitting material (K), ϕ is work function of emitting material (J), k_B is the Boltzmann constant ($J K^{-1}$). $A_G = 1.2 \times 10^{-6} A m^{-2} K^{-2}$ [45,46].

Using the maximum emission current of $48.7 \mu\text{A}$, corresponding to an emission temperature $745 \text{ }^\circ\text{C}$, a work function of 3.31 eV is recorded. This is close to the literature value of $3.1 - 3.3 \text{ eV}$ (depending on growth conditions) [47].

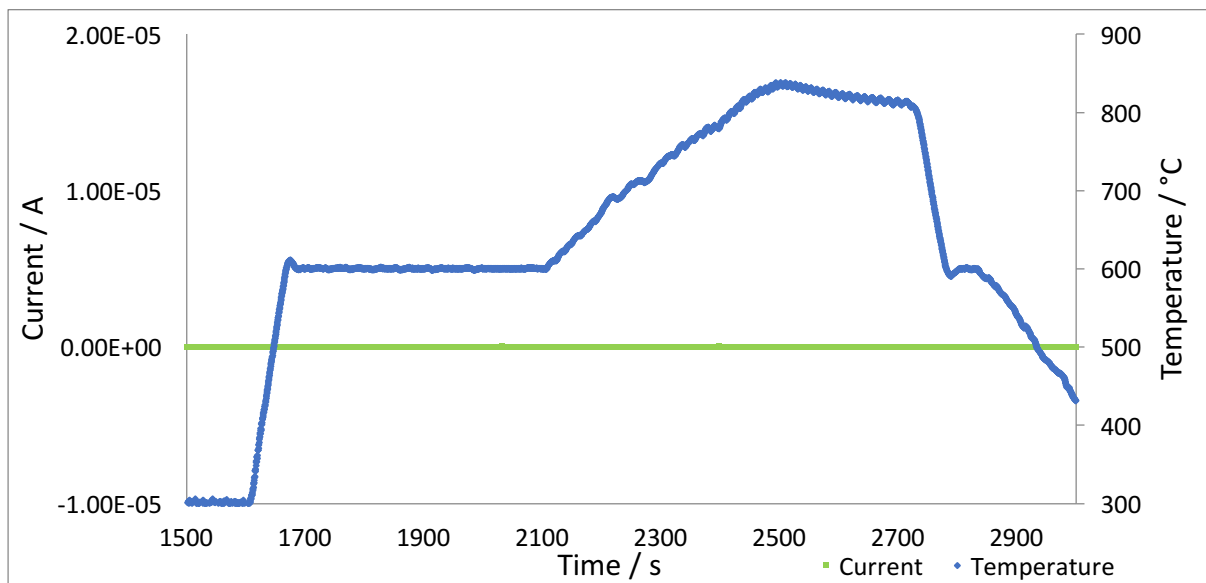


Figure 36: Thermionic electron emission for Ti-O terminated N9

Thermionic emission current was tested for N9 even when there was no Ti deposited onto the oxidised diamond film. The surface was still oxygen terminated and even when the laser reached its maximum output (correlating to a temperature of $837 \text{ }^\circ\text{C}$), there was still no electron emission. This is due to oxygen terminated diamond having a PEA rather than NEA and so has a higher work function than intrinsic diamond.

4. Conclusion

Nitrogen and boron doped diamond samples were grown using the appropriate CVD diamond growth techniques. The growth quality was assessed visually by using an optical microscope and spectroscopically by using Raman laser spectroscopy. Certain diamond films of interest were analysed further using scanning electron microscopy due to the electron beam having a smaller wavelength than visible light, hence it is possible to see more intricate detail on the diamond surface.

Chosen samples were suitably terminated using an oxygen or hydrogen plasma. The work functions of the samples were measured using the energy-filtered UPS work function mapping facility. Oxygen terminations yielded a positive electron affinity and hydrogen terminations yielded a negative electron affinity, as stated in the literature. It was experimentally confirmed that hydrogen terminated diamond is inadequate for possible future thermionic energy conversion sources as hydrogen desorbs from the surface at a relatively low temperature, changing the surface from inducing a negative electron affinity to a positive electron affinity. Titanium oxide theoretically looks like a promising diamond surface termination for low energy thermionic emission as it forms a stable oxide, withstanding temperatures far higher than hydrogen termination, and induces a larger negative electron affinity, hence exhibiting a low work function surface.

Unfortunately, due to time constraints on the project, no titanium was deposited onto the oxygen terminated diamond surface. It was hoped that experimentally depositing titanium onto oxygen terminated diamond would induce a negative electron affinity, hence significantly reducing the work function of the surface. Installing the appropriate metal deposition chamber on the NanoESCA should hopefully be completed in the near future and so the appropriate analysis methods can be carried out on titanium oxide terminated diamond.

4.1. Future Work

Depositing titanium onto the oxygen terminated diamond surface in the newly installed NanoESCA chamber to achieve a monolayer coverage on the diamond is the first procedure to complete in the future. The amount of surface coverage of titanium oxide could also be altered, testing for thermionic emission and see how the emission current varies for different coverages. The samples could be annealed at various different temperatures with XPS and work function mapping carried out for each sample. The most promising of samples would be then tested for thermionic emission. This would show if annealing the sample has the same effect on titanium oxide surfaces as it does with lithium oxide surfaces. It would also help migration across the surface to encourage an even coverage. Any variation that shows a reduced work function but is more thermally stable than hydrogen should be experimented on further to see if it could be a potential for thermionic emission sources.

Another area to investigate at would be repeating the experiments for scandium, zirconium, and vanadium to see if Tiwari *et al.*'s predictions were correct. The three metals surround titanium in the periodic table and so they are all similar in size and electronegativity. Tiwari *et al.* also reported that the metals form stable metal oxides and so could potentially be an area of interest for thermionic energy conversion source by exhibiting a low work function [29,30].

References

- [1] F. A. M. Koeck, R. J. Nemanich, A. Lazea, K. Haenen, *Diam. Relat. Mater.*, 2009, **18**, 789–791
- [2] M. Suzuki, T. Ono, N. Sakuma, T. Sakai, *Diam. Relat. Mater.*, 2009 **18**, 1274-1277
- [3] R. F. Davis, Z. Sitar, B. E. Williams, H. S. Konh, H. J. Kim, J. W. Palmour, J. A. Edmond, J. Ryu, J. T. Glass, C. H. Carter Jr., *Mater. Sci. & Eng. B*, 1988, **1**, 77-104
- [4] M. Z. Othman, PhD thesis, University of Bristol, **2014**
- [5] F. A. M. Koeck, R. J. Nemanich, *Diam. Relat. Mater.*, 2005, **14**, 2051-2054
- [6] D. B. Go, J. R. Haase, J. George, J. Mannhart, R. Wanke, A. Nojeh, R. Nemanich, *Front. Mech. Eng.*, 2017, **3**, 1-17
- [7] Q. Zhou, Z. Fang, J. Li, M. Wang, *Microporous and Mesoporous Materials*, 2015, **202**, 22–35
- [8] R. Kalish, *Carbon*, 1999, **37**, 781–785
- [9] P. Atkins, J. Paula, *Atkin’s Physical Chemistry.*, Oxford University Press, Oxford, 2014
- [10] M. Weller, T. Overton, J. Rourke, F. Armstrong, *Inorganic Chemistry* Oxford University Press, Oxford, 2014
- [11] S. A. Kajihara, A. Antonelli, J. Bernholc, R. Car, *Phys. Rev. Lett.* 1991, **66**, 2010-2013
- [12] C. J. H. Wort, R. S. Balmer, *Mater. Today*, 2008, **11**, 22-28
- [13] A. Mainwood, *J. Mater. Sci.: Mater. Electron*, 2006, **17**, 453–458
- [14] P. W. May, *Phil. Trans. R. Soc. Lond. A*, 2000, **358**, 473-495
- [15] S. Koizumi, M. Kamo, Y. Sato, S. Mitea, A. Sawabe, A. Reznik, C. Uzan-Saguy, R. Kalish, *Diam. Relat. Mater.*, 1998, **7**, 540-544
- [16] M. Pomorski, PhD thesis, Frankfurt University, **2008**
- [17] W. Chen, D. Qi, X. Gao, A. T. S. Wee, *Progress in Surface Science*, 2009, **84**, 279–321
- [18] K. M. O’Donnell, T. L. Martin, N. A. Fox, D. Cherns, *Mater. Res. Soc. Symp. Proc.*, 2011, **1282**, 163 - 168
- [19] J. B. Cui, J. Ristein, and L. Ley, *Phys. Rev. Lett.*, 1998, **81**, 429-432
- [20] W. F. Paxton, A. Steigerwald, M. Howell, N. Tolk, W. P. Kang, and J. L. Davidson, *Appl. Phys. Lett.*, 2012, **101**, 243509
- [21] K. M. O’Donnell, T. L. Martin, M. T. Edmonds, A. Tadich, L. Thomsen, J. Ristein, C. I. Pakes, N. A. Fox, L. Ley, *Phys. Status Solidi A*, 2014, **211**, 2209-2222
- [22] O’Donnell, M. T. Edmonds, J. Ristein, A. Tadich, L. Thomsen, Q. Wu, C.I. Pakes, L. Ley, *Adv. Funct. Mater.*, 2013, **23**, 5608-5614
- [23] K. M. O’Donnell, T. L. Martin, N. A. Fox, D. Cherns, *Phys. Rev. B*, 2010, **82**, 115303
- [24] M. C. James, A. Croot, P. W. May, N. L. Allan, *J. Phys: Condens. Matter*, 2018, **30**, 235002
- [25] T. L. Martin, PhD thesis, University of Bristol, **2011**
- [26] I. L. Krainisky, V. M. Asnin, G. T. Mearini, J. A. Dayton, Jr., *Phys. Rev. B*, 1996, **53**, 7650-7653
- [27] C. Bandis, B. B. Pate, *Phys. Rev. B*, 1995, **52**, 12056-12071
- [28] J. L. Nie, H. Y. Xiao, X. T. Zu, F. Gao, *Chem. Phys.*, 2006, **326**, 308-314
- [29] A. K. Tiwari, J. P. Goss, P. R. Briddon, A. B. Horsfall, N. G. Wright, R. Jones, M. J. Rayson, *Europhys. Lett.*, 2014, **108**, 46005
- [30] A. K. Tiwari, J. P. Goss, P. R. Briddon, N. G. Wright, A. B. Horsfall, M. J. Rayson, *Phys. Status Solidi A*, 2012, **209**, 1697-1702
- [31] K. M. O’Donnell, M. T. Edmonds, A. Tadich, L. Thomsen, A. Stacey, A. Schenk, C. I. Pakes, L. Ley, *Phys. Rev. B*, 2015, **92**, 035303
- [32] K. M. O’Donnell, T. L. Martin, N. L. Allan, *Chem. Mater.*, 2015, **27**, 1306-1315
- [33] A. K. Tiwari, PhD thesis, Newcastle University, **2013**
- [34] K. M. O’Donnell, Mch. T. Edmonds, J. Ristein, K. J. Rietwky, A. Tadich, L. Thomsen, C.I. Pakes, L. Ley, *J. Phys.: Condens. Matter*, 2014, **26**, 395008
- [35] S. Matsumoto, Y. Sato, M. Tsutsumi, N. Seteka, *J. Mater. Sci.*, 1982, **17**, 3106–3112
- [36] L. Nistor, J. Van Landuyt, V. Ralchenko, *Phys. Stat. Sol.*, 1999, **174**, 5-9
- [37] H. Kawarada, *Surface Sci. Report*, 1996, **26**, 205-259
- [38] J. A. Smith, PhD thesis, Bristol University, **2002**

- [39] M. Kamo, Y. Sato, S. Matsumoto, N. Setaka, *J. Crystal Growth*, 1983, **62**, 642-644
- [40] M. N. R. Ashfold, P. W. May, C. A. Rego, N. M. Everitt, *Chem. Soc. Rev.*, 1994, **23**, 21-30
- [41] K. Kobashi, A. Nakaue, J. T. Glass, I. M. Buckley-Golder, *Carbon*, 1990, **6**, 756-757
- [42] B. Miljevic, F. Hedayat, S. Stevanovic, K. E. Fairfull-Smith, S. E. Bottle, Z. D. Ristovski, *Aerosol Sci. And Tech.*, 2014, **48**, 1276-1284
- [43] J. D Andrade, *Surface and Interfacial Aspects of Biomedical Polymers*, Springer, Boston, 1985
- [44] B. V. Spitsyn, L. L. Bouilov, B. V. Derjaguin, *J. Crystal Growth*, 1981, **52**, 219-226
- [45] A.K. Vijn, P. Lenfant, *Can. J. Phys.*, 1973, **51**, 111-113
- [46] Y. N. Yang, D. D. Coon, P. F. Shepard, *Appl. Phys. Lett.*, 1984, **45**, 752-754
- [47] L. Diederich, O. M. Küttel, P. Aebi, L. Schlapbach, *Surface Sci.*, 1998, **418**, 219-239
- [48] S. Praver, R. J. Nemanich, *Phil. Trans. R. Soc. Lond. A*, 2004, **362**, 2537 – 2565
- [49] A. C. Ferrari, J. Robertson, *Phys. Rev. B*, 2001, **63**, 121405
- [50] J. E. Butler, Y. A. Mankelevich, A. Cheesman, J. Ma, M. N. R. Ashfold, *J. Phys.: Condens. Matter*, 2009, **21**, 364201
- [51] S. Jin, T. D. Moustakas, *Appl. Phys. Lett.*, 1994, **65**, 403-405
- [52] J. E. Gerbi, O. Auciello, J. M. Gibson, J. Birrell, D. M. Gruen, J. A. Carlisle, *J. Appl. Phys.*, 2003, **93**, 5606-5612
- [53] R. J. Zhang, S. T. Lee, Y. W. Lam, *Diam. Relat. Mater.*, 1996, **5**, 1288-1294
- [54] P. W. May, W. J. Ludlow, M. Hannaway, P. J. Heard, J. A. Smith, K. N. Rosser, *Diam. Relat. Mater.*, 2008, **17**, 105-117
- [55] J. W. Ager, W. Walukiewicz, M. McCluskey, M. A. Plano, M. I. Landstrass, *Appl. Phys. Lett.*, 1995, **66**, 616-618.
- [56] O.A. Williams, M. Neslède, *Phys. Stat. Sol. A*, 2006, **203**, 3375-3386
- [57] J. I. B. Wilson, J. S. Walton, G. Beamson, *J. Electron Spectros. And Relat. Phenomena*, 2001, **121**, 183-201
- [58] F. Jansen, M. A. Machonkin, D. E. Kuhman, *J. Vac. Sci. And Technol. A*, 1990, **8**, 3785-3790
- [59] O. Renault, A. Chabli, *AIP Conference Proceedings*, 2007, **931**, 502-506
- [60] P. W. May, Y. A. Mankelevich, *J. Phys. Chem. C*, 2008, **112**, 12432-12441
- [61] T. Liu, D. Raabe, *Appl. Phys. Lett.*, 2009, **94**, 021119
- [62] A. Tallaire, A.T. Collins, D. Charles, J. Achard, R. Sussmann, A. Gicquel, M.E. Newton, A.M. Edmonds, R.J. Cruddace, *Diam. Relat. Mater.*, 2006, **15**, 1700-1707
- [63] H. Nagasaka, Y. Teranishi, Y. Kondo, T. Miyamoto, T. Shimizu, *e-J. Surf. Sci. Nanotech.*, 2016, **14**, 53-58
- [64] N.G. Ferreira, E. Abramof, E.J. Corat, N.F. Leite, V.J. Trava-Airoldi, *Diam. Relat. Mater.*, 2001, **10**, 750-754

Appendix

6.1. Raman Spectroscopy

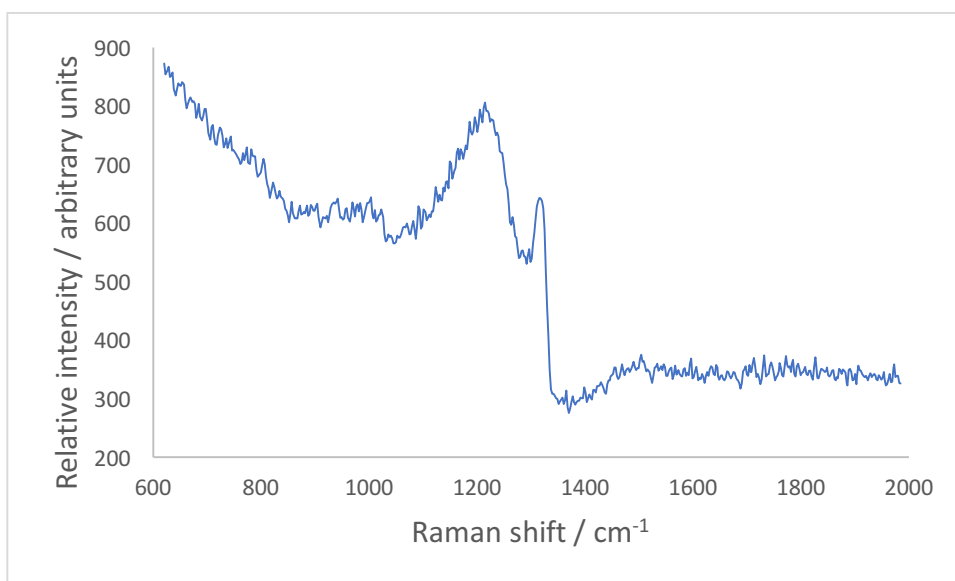


Figure 37: Raman spectrum for B1, taken on the Renishaw 2000 laser Raman spectrometer

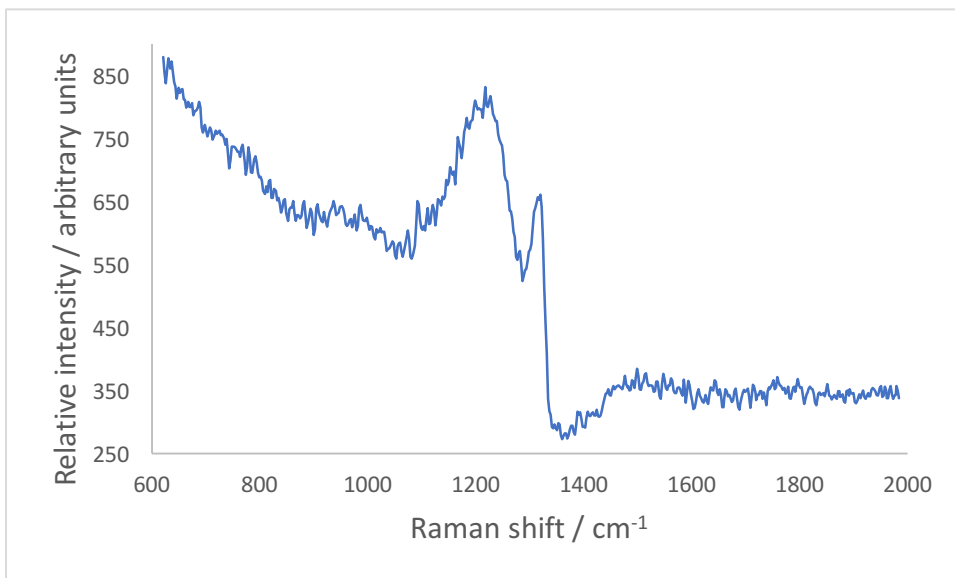


Figure 38: Raman spectrum for B4, taken on the Renishaw 2000 laser Raman spectrometer

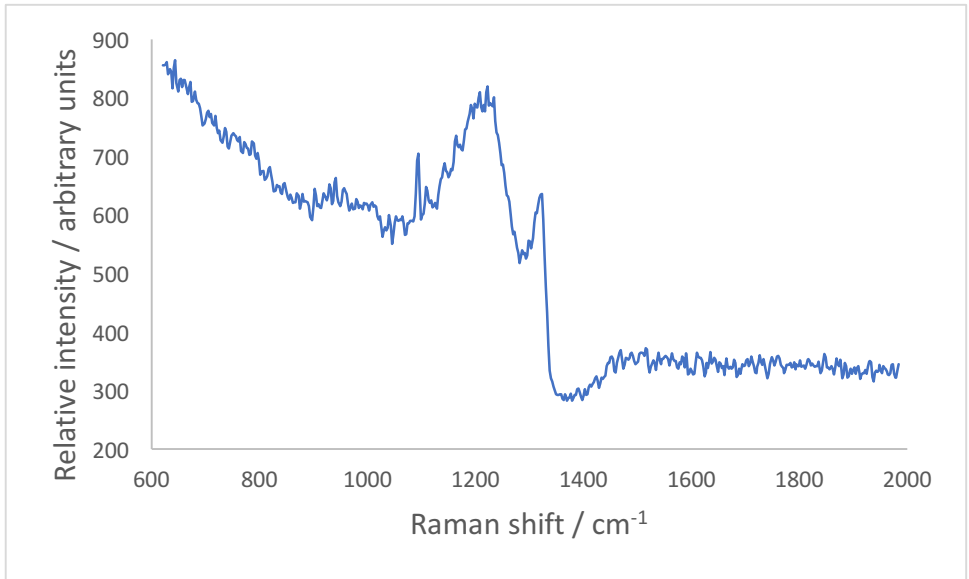


Figure 39: Raman spectrum for B5, taken on the Renishaw 2000 laser Raman spectrometer

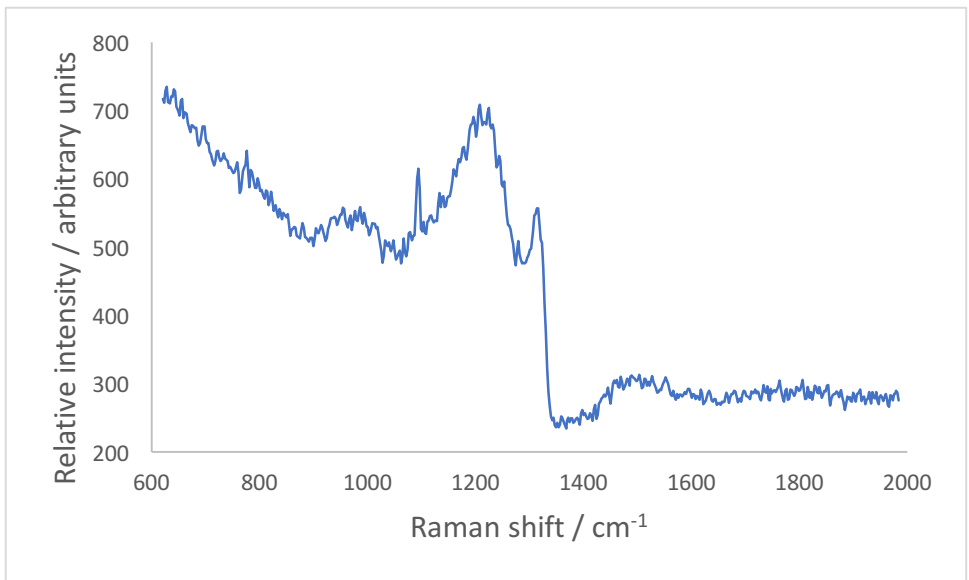


Figure 40: Raman spectrum for B6, taken on the Renishaw 2000 laser Raman spectrometer

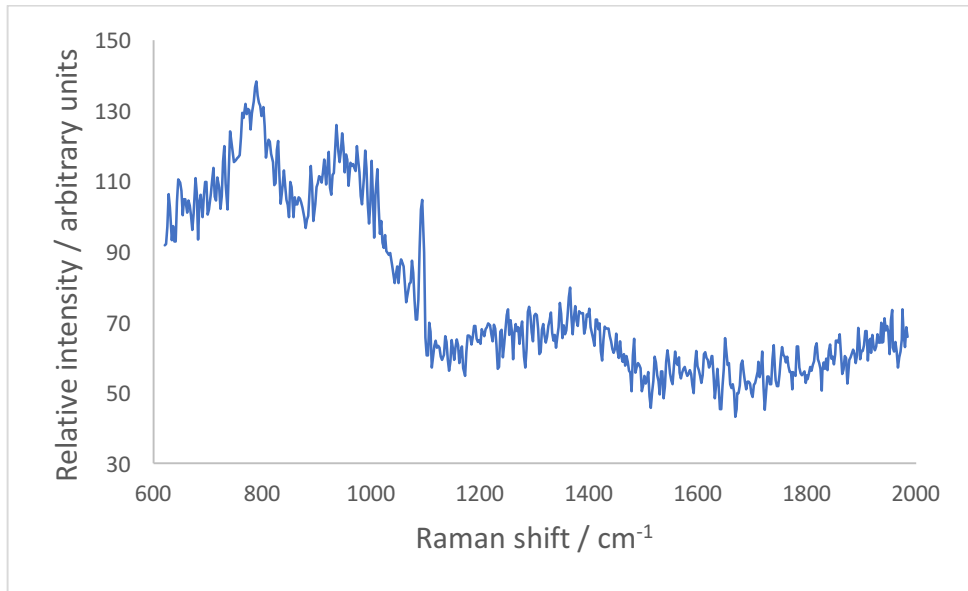


Figure 41: Raman spectrum for N1, taken on the Renishaw 2000 laser Raman spectrometer

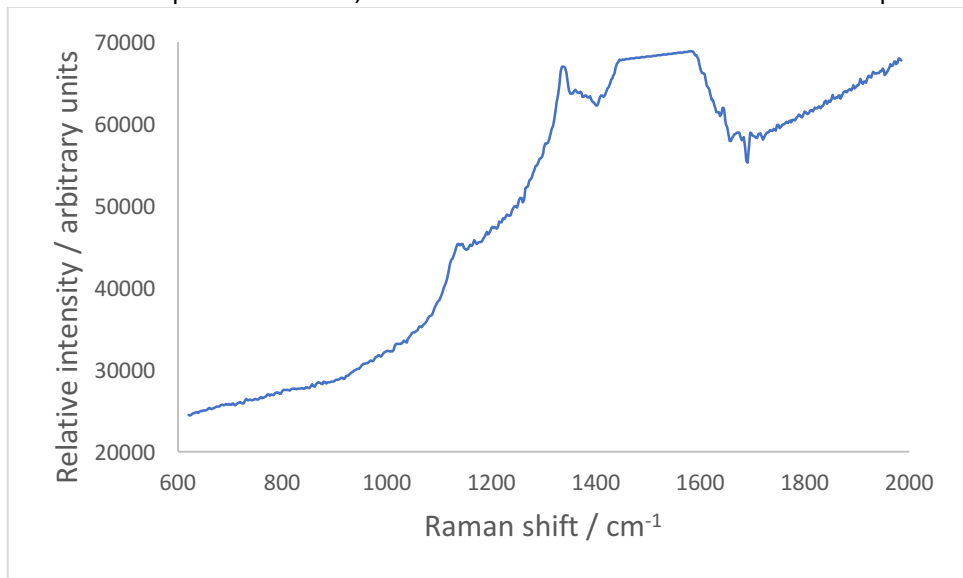


Figure 42: Raman spectrum for N2, taken on the Renishaw 2000 laser Raman spectrometer

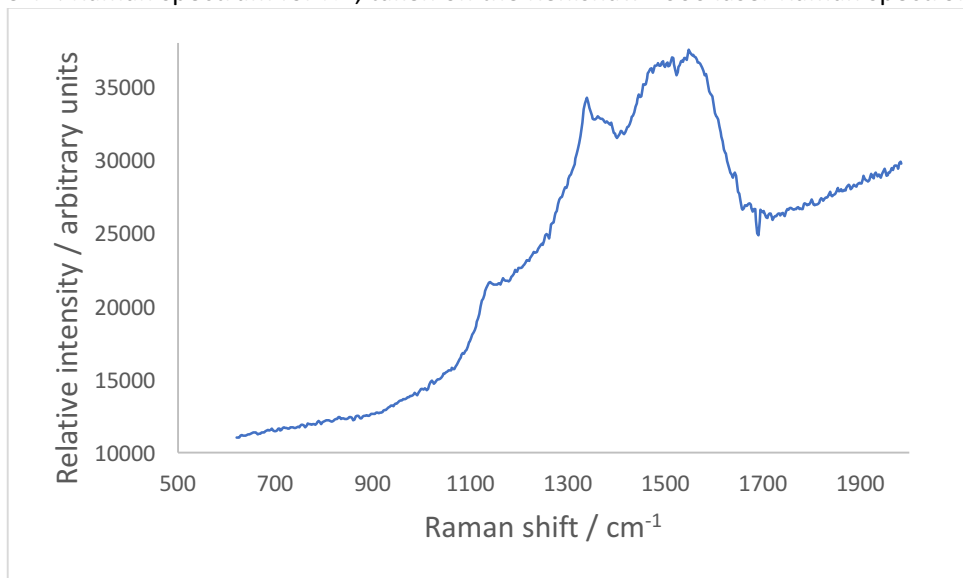


Figure 43: Raman spectrum for N3, taken on the Renishaw 2000 laser Raman spectrometer

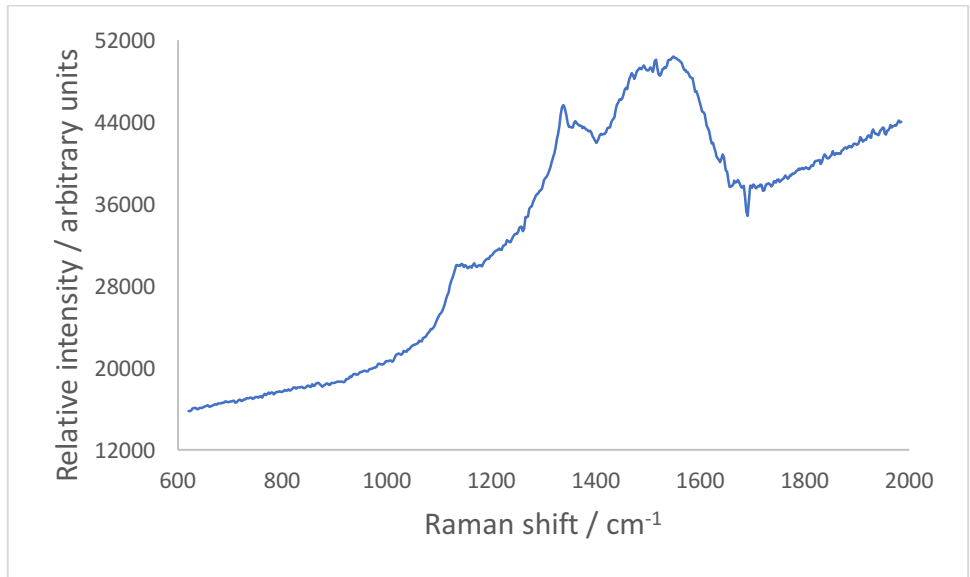


Figure 44: Raman spectrum for N4, taken on the Renishaw 2000 laser Raman spectrometer

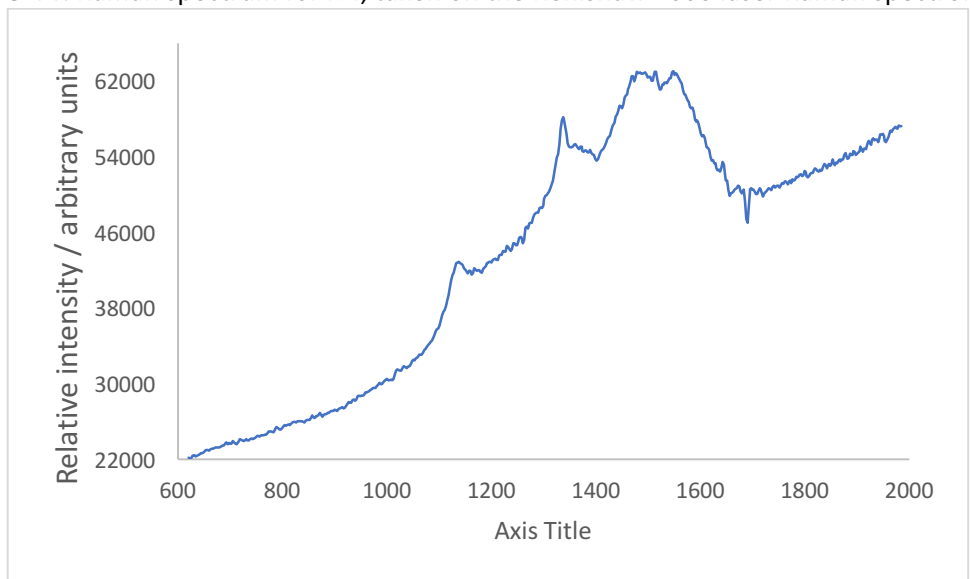


Figure 45: Raman spectrum for N5, taken on the Renishaw 2000 laser Raman spectrometer

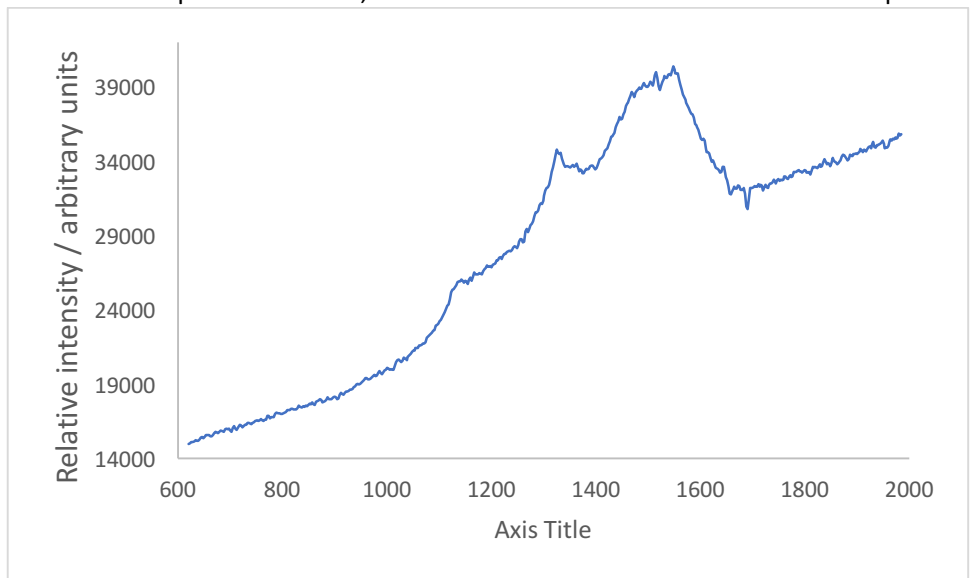


Figure 46: Raman spectrum for N6, taken on the Renishaw 2000 laser Raman spectrometer

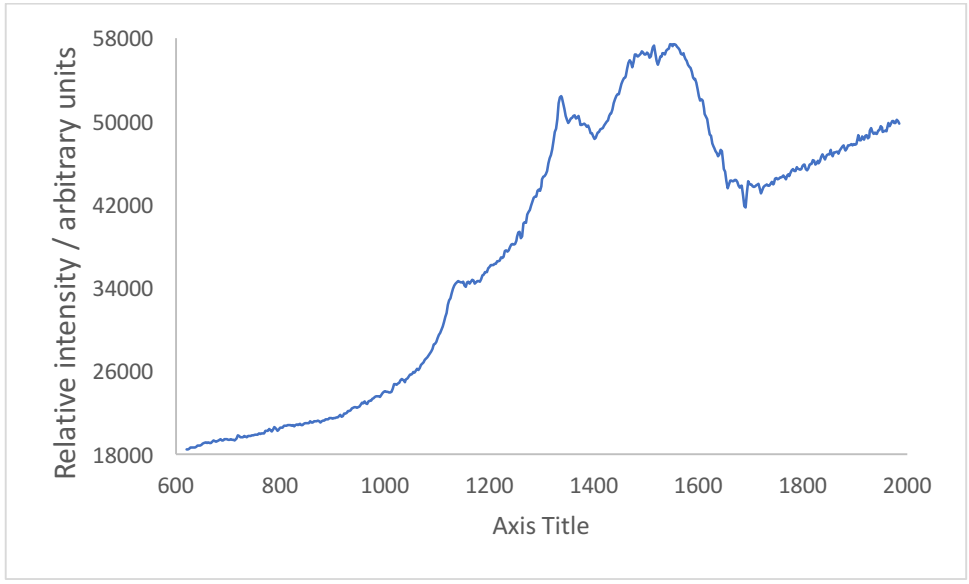


Figure 47: Raman spectrum for N7, taken on the Renishaw 2000 laser Raman spectrometer

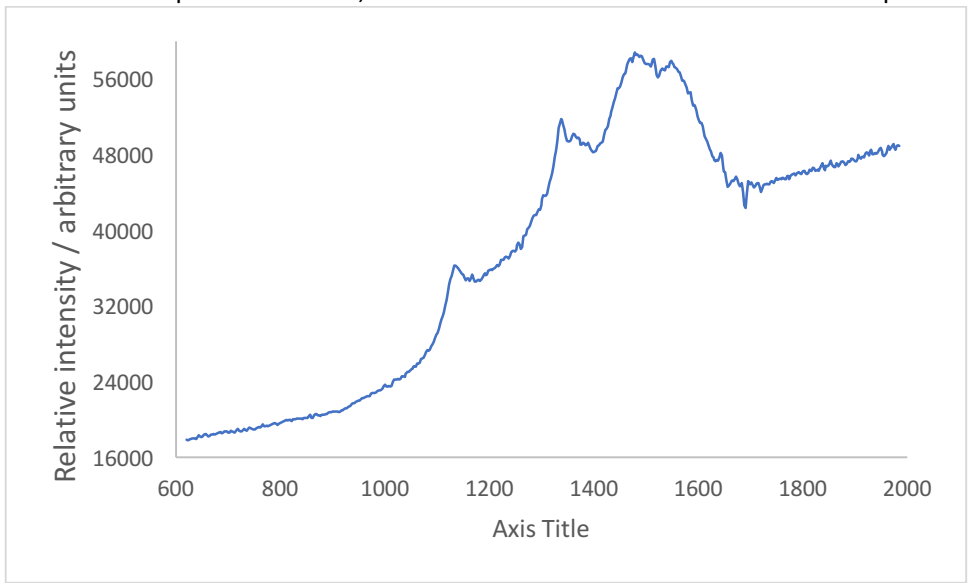


Figure 48: Raman spectrum for N8, taken on the Renishaw 2000 laser Raman spectrometer

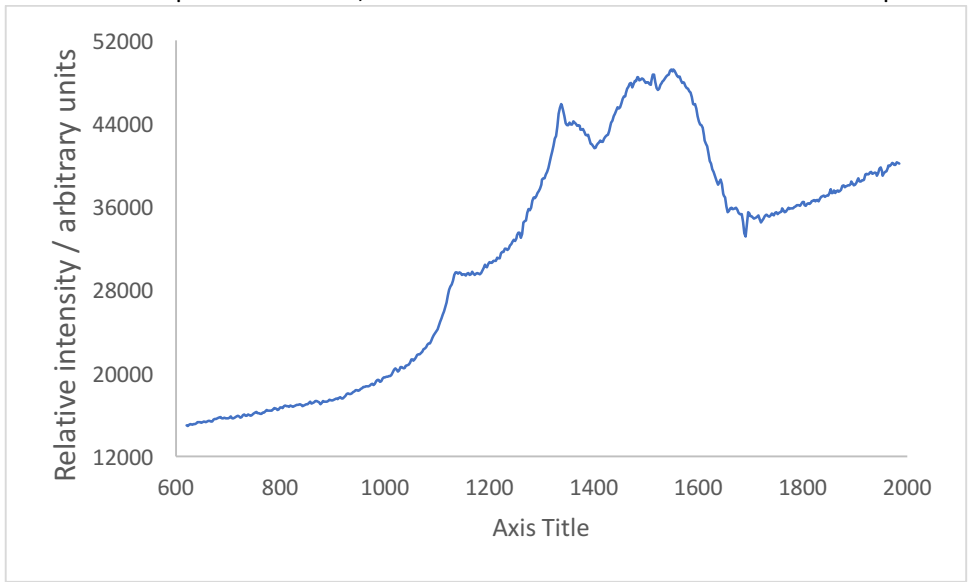


Figure 49: Raman spectrum for N11, taken on the Renishaw 2000 laser Raman spectrometer

6.2. Optical Microscope Images



Figure 50: Optical microscope image taken of samples B1.

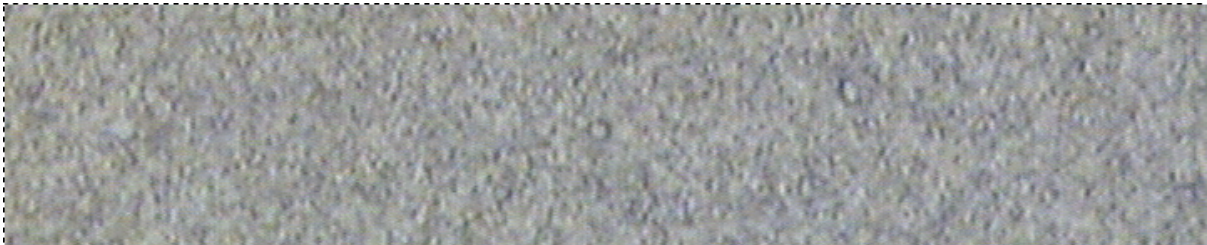


Figure 51: Optical microscope image taken of samples B2.



Figure 52: Optical microscope image taken of samples B4.

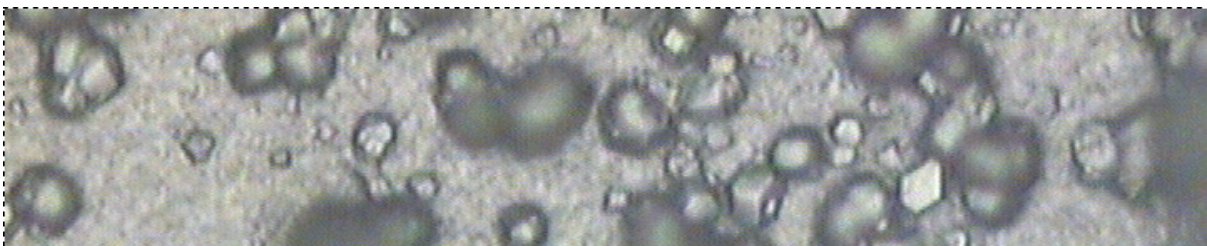


Figure 53: Optical microscope image taken of samples B5.



Figure 54: Optical microscope image taken of samples B6.

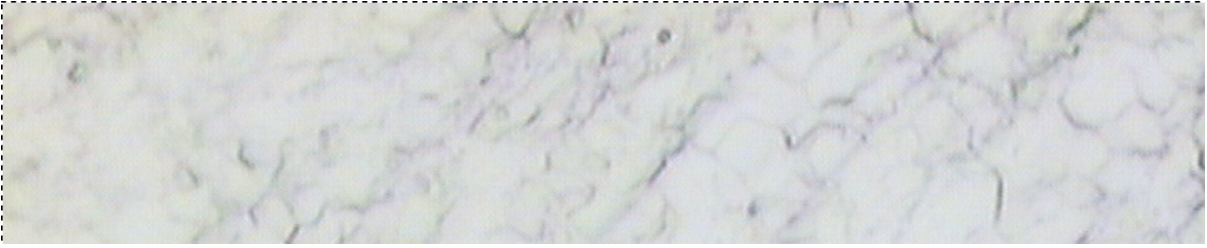


Figure 55: Optical microscope image taken of samples N1.



Figure 56: Optical microscope image taken of samples N2.



Figure 57: Optical microscope image taken of samples N3.



Figure 58: Optical microscope image taken of samples N4.



Figure 59: Optical microscope image taken of samples N5.



Figure 60: Optical microscope image taken of samples N8.



Figure 61: Optical microscope image taken of samples N9.



Figure 62: Optical microscope image taken of samples N11.

6.3. XPS Survey

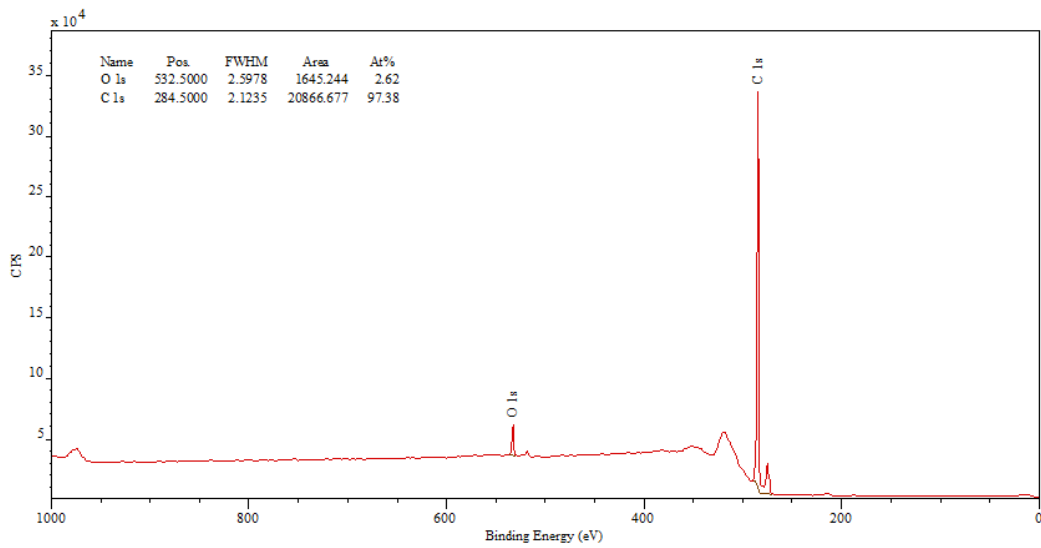


Figure 63: CasaXPS survey spectrum for B2.

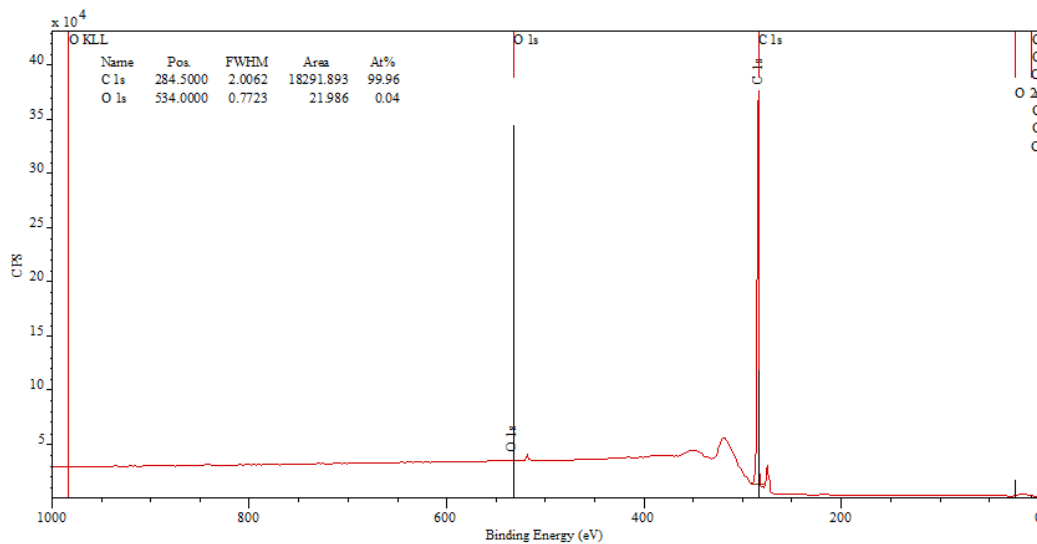


Figure 64: CasaXPS survey spectrum for B3.

6.4. Scanning Electron Microscopy Images

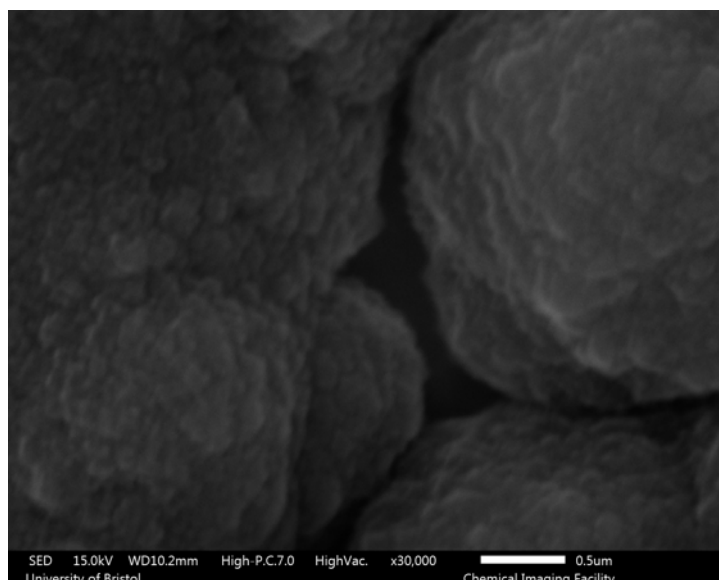


Figure 65: SEM image of N2. Magnifications of x30,000

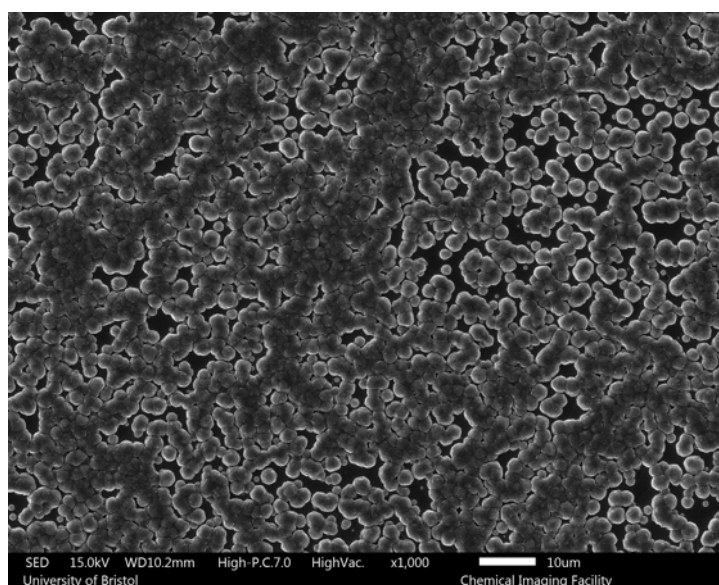


Figure 66: SEM image of N2. Magnifications of x1000

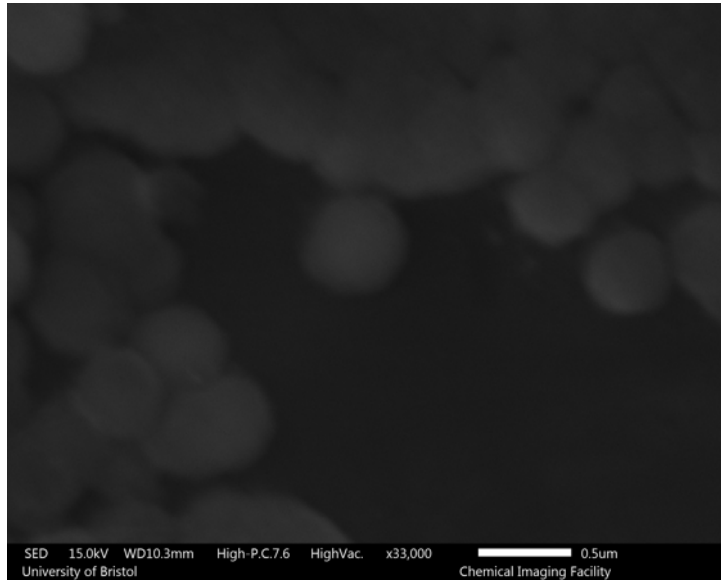


Figure 67: SEM image of N6. Magnifications of x33,000

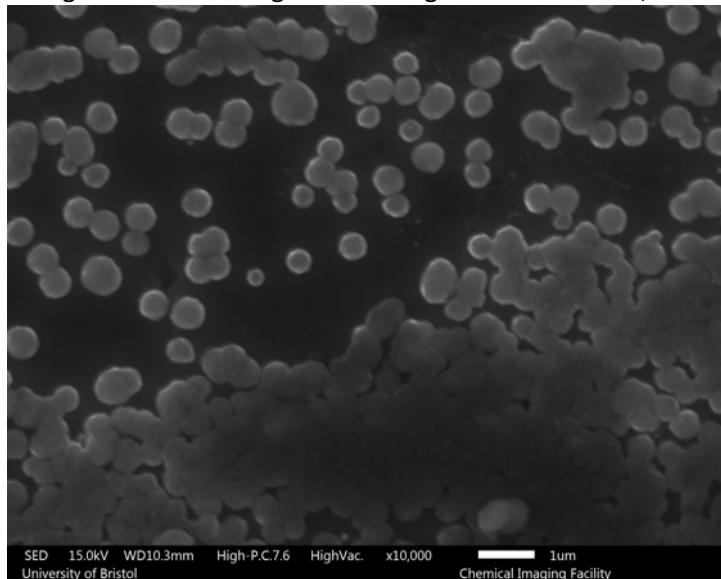


Figure 68: SEM image of N6. Magnifications of x10,000

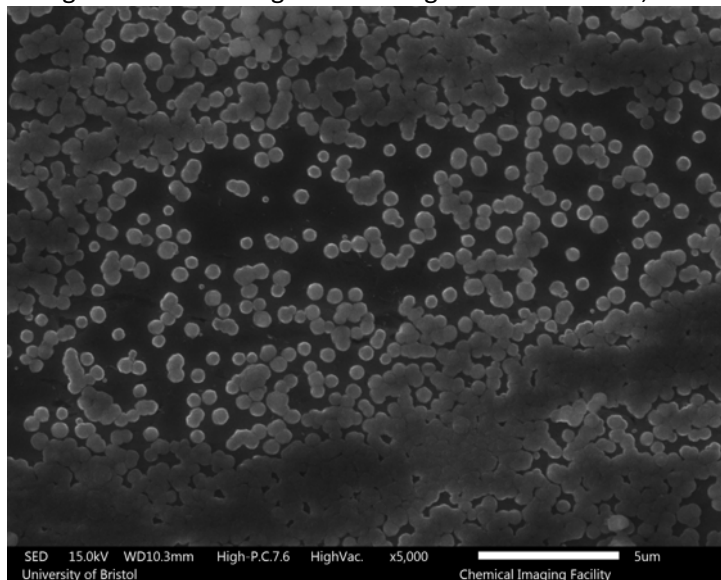


Figure 69: SEM image of N6. Magnifications of x5,000

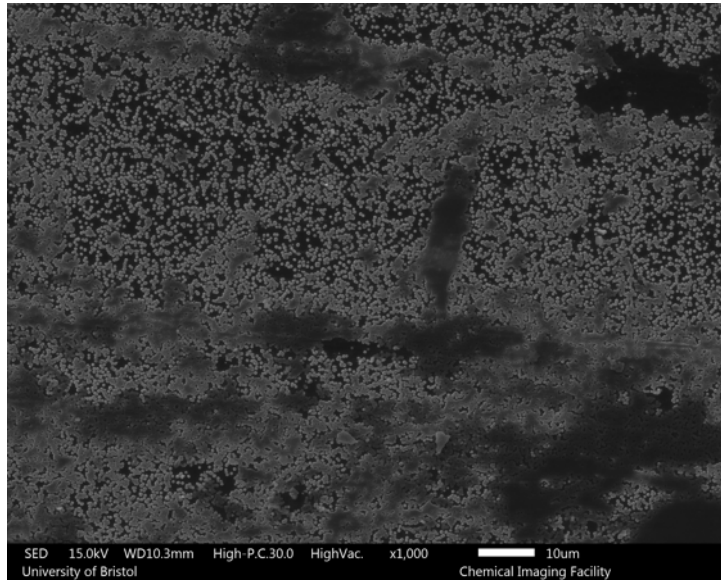


Figure 70: SEM image of N6. Magnifications of x1000

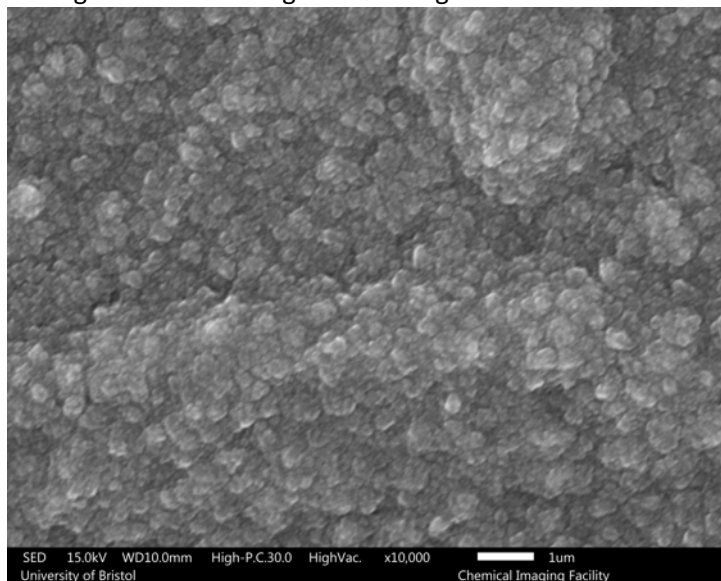


Figure 71: SEM image of N7. Magnification of x10,000

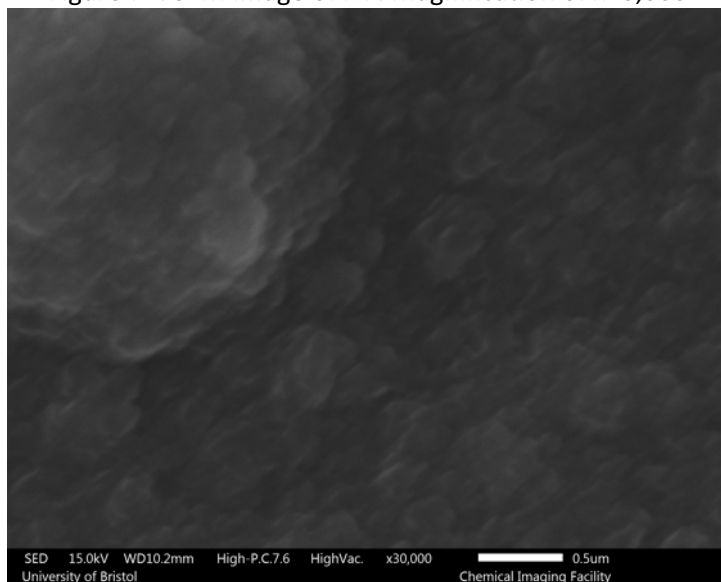


Figure 72: SEM image of N9. Magnification of x30,000

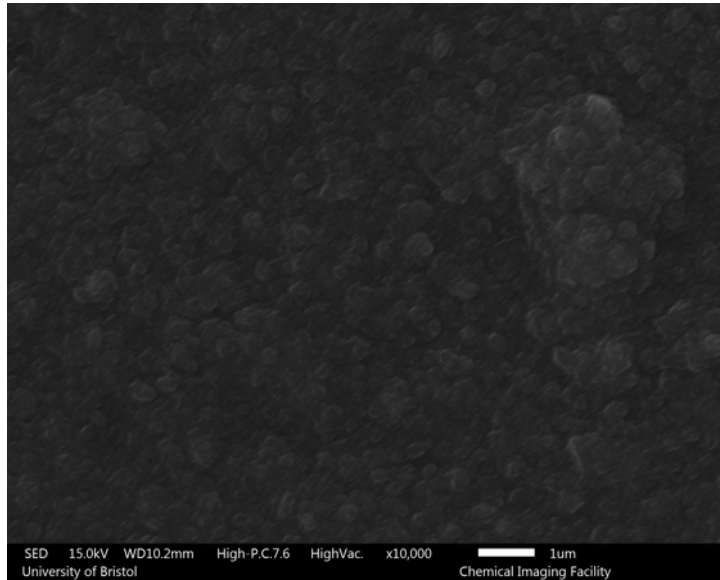


Figure 73: SEM image of N9. Magnification of x10,000

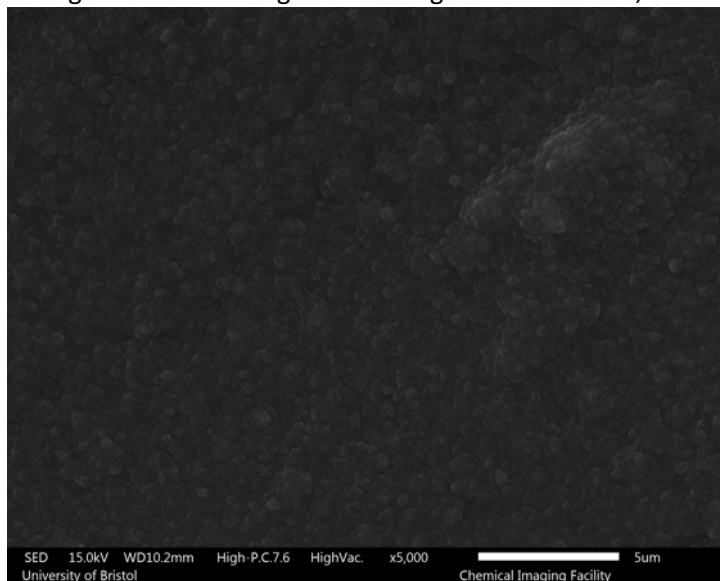


Figure 74: SEM image of N9. Magnification of x5,000

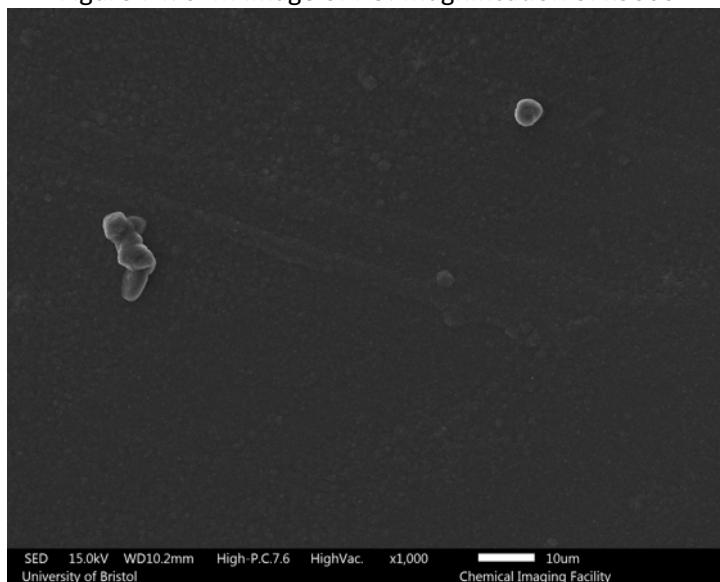


Figure 75: SEM image of N9. Magnification of x1,000

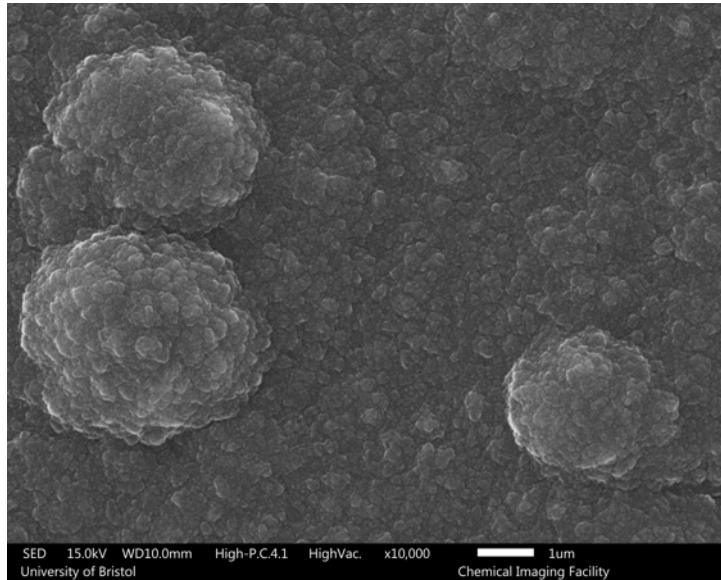


Figure 76: SEM image of N11. Magnification of x10,000

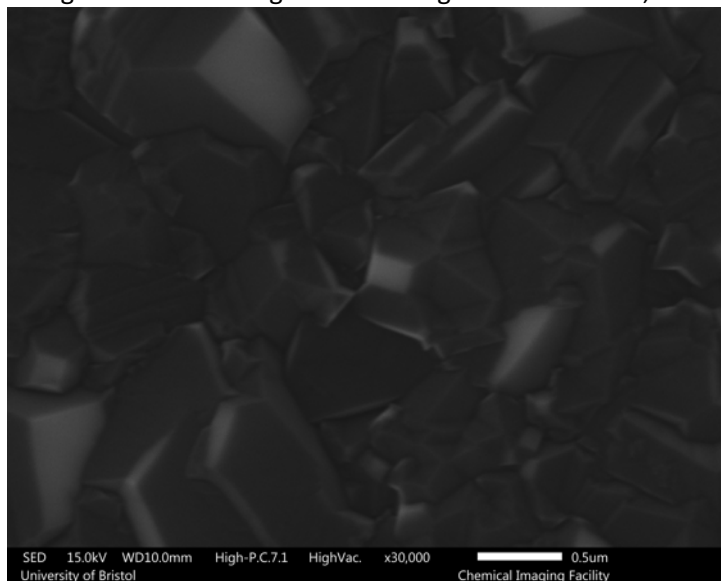


Figure 77: SEM image of B4. Magnification of x30,000

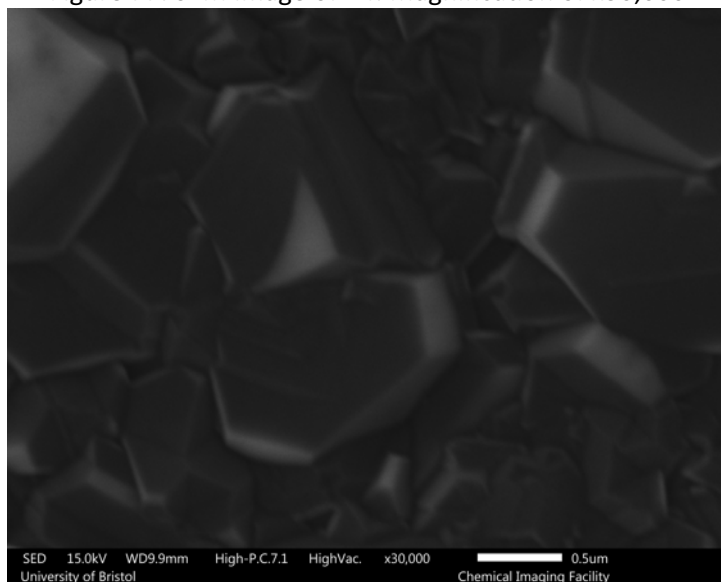


Figure 78: SEM image of B6. Magnification of x30,000

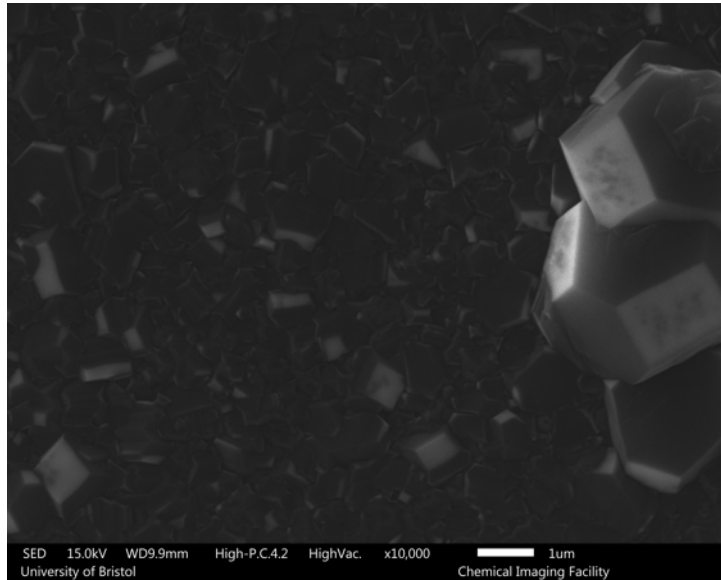


Figure 79: SEM image of B6. Magnification of x10,000

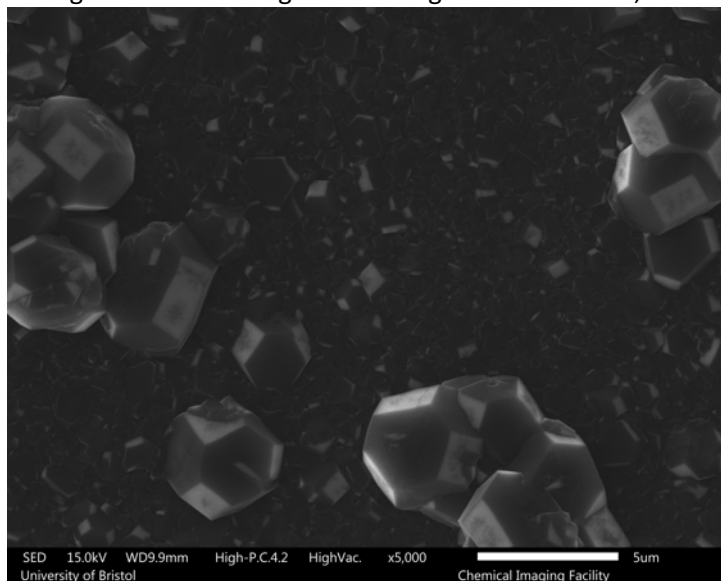


Figure 80: SEM image of B6. Magnification of x5000

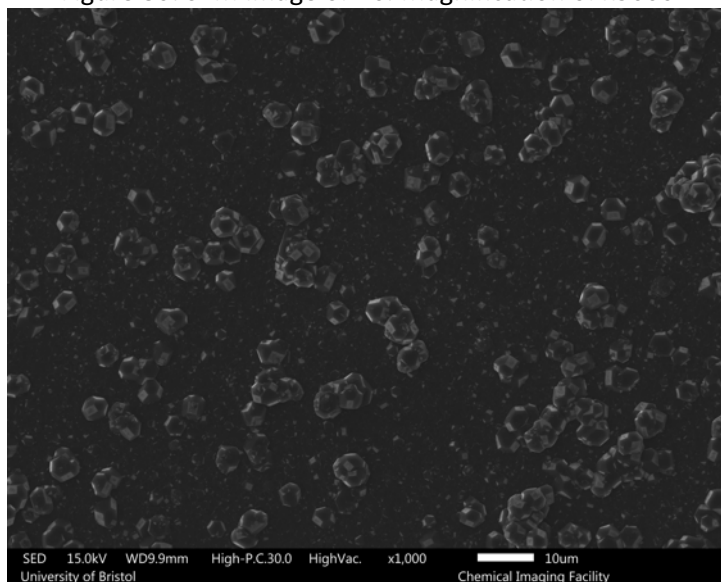


Figure 81: SEM image of B6. Magnification of x1000